Nuclear Instruments and Methods in Physics Research A 1075 (2025) 170361

Contents lists available at ScienceDirect

Nuclear Inst. and Methods in Physics Research, A

journal homepage: www.elsevier.com/locate/nima

Full Length Article

Microscopic and spectroscopic analysis of ion-irradiated molecular-plated thin films for superheavy element production

C.-C. Meyer [a,b,*], E. Artes [a,b,c], M. Bender [c,g], J. Brötz [d], Ch.E. Düllmann [a,b,c], T. Gouder [e], E. Jäger [c], B. Kindler [c], S. Herz [a], B. Lommel [c], M. Major [d], C. Mokry [a,b], F. Munnik [f], M. Rapps [a,1], D. Renisch [a,b], J. Runke [c], A. Seibert [e], C. Trautmann [c,d], N. Trautmann [a], O. Walter [e], A. Yakushev [c]

[a] Department Chemie - Standort TRIGA, Johannes Gutenberg-Universität Mainz, Fritz-Strassmann-Weg-2, 55128 Mainz, Germany
[b] Helmholtz-Institut Mainz, Staudingerweg 18, 55128 Mainz, Germany
[c] GSI Helmholtzzentrum für Schwerionenforschung GmbH, Planckstraße 1, 64291 Darmstadt, Germany
[d] Technische Universität Darmstadt - Materialwissenschaft, Peter-Grünberg-Straße 2, 64287 Darmstadt, Germany
[e] European Commission, Joint Research Centre (JRC) - Karlsruhe, Hermann-von-Helmholtz-Platz 1, 76344 Eggenstein-Leopoldshafen, Germany
[f] Helmholtz-Zentrum Dresden-Rossendorf, Ion Beam Center, Bautzner Landstraße 400, 01328 Dresden, Germany
[g] Hochschule RheinMain, Am Brückweg 26, 65428 Rüsselsheim, Germany

ARTICLE INFO

Keywords:
Target preparation
Molecular plating
Electrochemical deposition
Raman microscopy
Lanthanide

ABSTRACT

The heaviest known elements are produced via fusion reactions by bombarding actinide targets with intense heavy ion beams. The production of actinide targets relies mainly on the molecular plating (MP) technique. Long-term stability of MP produced targets is typically achieved by a conditioning procedure, in which fresh targets are exposed to successively increasing beam intensities. This leads to non-trivial physical and chemical transformations, which are presently poorly understood. To shed light on processes in the initial irradiation stage, we irradiated thin Tm MP films with Cl and Au ions of different fluences, with the latter ranging from 10^{10} $\frac{\text{ions}}{\text{cm}^2}$ to 10^{14} $\frac{\text{ions}}{\text{cm}^2}$, and analyzed their morphology and composition by a variety of microscopic, spectroscopic and ion beam techniques. The study was conducted on lanthanide targets, which serve as non-radioactive analogues for heavy actinide targets. Combining the results of several methods, we conclude that the MP thin films consist of a mixture of carbonates and formates. Under irradiation, these films transform into amorphous oxides with embedded carbon clusters.

1. Introduction

In recent decades, remarkable progress has been made in the production of superheavy elements (SHE) [1–4]. For this purpose, targets of the heaviest actinides, such as ^{242}Pu [5], ^{243}Am [6,7] and ^{249}Bk [8], were irradiated with ^{48}Ca ions at heavy-ion accelerators. Actinide targets are typically produced by molecular plating (MP), where the desired actinides are electrochemically deposited as thin films ($\frac{\mu g}{cm^2}$) on very thin Ti foils (1.5 µm to 2.3 µm) [9]. The MP method presents a critical limitation to experimental progress in the field [10–12], as it is unable to produce targets of sufficient thickness to cover the full useful width of the excitation functions [12,13]. Given the large solid angle acceptances of current recoil separators and the overall detection efficiency of current experimental setups, production rates can almost exclusively be increased by using more intense ion beams and/or thicker targets [14–18]. Both options require the development of actinide targets with improved stability. At present, the MP method is unable to take full advantage of the higher beam intensities that are now available [2,10,11]. A prerequisite for new target developments is a profound understanding of the existing MP method and the behavior of MP targets in the ion beam. Despite numerous publications on the MP method, the exact process of molecular plating and thus the properties of the MP thin films remain rather unknown. A brief current literature overview can be found in [19].

MP targets have sometimes limited stability after production and are usually conditioned on-line [20,21] using progressively increasing heavy-ion beam intensities over the course of a few hours. Bake-in procedures at GSI are done at earliest available beamtimes after target fabrication or alternatively directly at the beginning of a SHE production run, e.g., during adjustments of the experimental setup.

* Corresponding author at: Department Chemie - Standort TRIGA, Johannes Gutenberg-Universität Mainz, Fritz-Strassmann-Weg-2, 55128 Mainz, Germany.
E-mail address: cmeyer02@uni-mainz.de (C.-C. Meyer).
[1] Deceased.

https://doi.org/10.1016/j.nima.2025.170361
Received 14 July 2024; Received in revised form 12 February 2025; Accepted 20 February 2025
Available online 12 March 2025

Examples for this are ^{243}Am targets used at TASCA (TransActinide Separator and Chemistry Apparatus) in 2012 for spectroscopy experiments on Mc (Z = 115) decay chains [6], and later Nh (Z = 113) and Mc (Z = 115) chemistry studies [7]. Or ^{244}Pu targets produced in 2014 for chemical studies of Fl (Z = 114) [22,23] as well as for Fl nuclear spectroscopy studies [5,24,25]. Without conditioning, the actinide thin films may experience limited adherence to their backing. After bake-in, though, even storage for months or years under normal conditions in air has no effect on the performance of such baked-in targets. The chemical processes involved in different conditioning procedures are still unknown, but attempts have already been made to develop offline equipment in order to make progress in this field without irradiation time at an accelerator [26,27].

For SHE production experiments, special MP targets are fabricated from actinide isotopes, which usually are α-emitters [28]. α-Spectroscopic studies of the target layer show that the width of the α-lines undergoes a change [20,21] as the beam fluence increases, indicating a radiation-induced alteration in the material. These modifications are initiated by a relatively low ion dose and then remain constant throughout the entire SHE production experiment. Changes in the morphology of actinide thin films were also documented by photographic images [20,21], Atomic Force Microscopy (AFM) [29] and Scanning Electron Microscopy (SEM) [29]. Analytical methods have so far been limited to Energy Dispersive X-ray spectroscopy (EDX) [29] and conventional X-ray Diffraction (XRD) [29]. Both methods are challenged by the peculiarities of the current MP target technology and characterized by a poor signal-to-noise ratio. Initial research using Raman spectroscopy on thin ion-irradiated lead films [26,27] as a model system for accelerator targets has demonstrated the conversion of carbonates into oxides.

A more detailed examination of MP-produced films and research into the conditioning process would benefit from access to state-of-the-art analytical techniques. Furthermore, the analysis of actinide films necessitates the use of licensed laboratories with the corresponding handling permits. To circumvent this issue, we thus replaced the actinides with lanthanide targets. Actinides elements with Z $\geq$95 are chemically very similar to lanthanides [30], rendering the latter ideal for initial studies and for the development of novel protocols for actinide target production [9,12,19]. The irradiation of lanthanide thin films serves as a preliminary stage for irradiation experiments on actinide thin films. Analyzing these films poses specific challenges due to their intricate morphology. Similar demands are present for both irradiated and non-irradiated films. The MP thin films produced and irradiated in this study were characterized using the following analytical methods (see Table 1):

(i) SEM to examine morphological alterations.
(ii) Various Ion Beam Analysis (IBA) techniques for elemental analysis, including Elastic Recoil Detection Analysis (ERDA), Rutherford Backscattering Spectrometry (RBS) and Particle-Induced X-ray Emission (PIXE).
(iii) Raman and infrared (IR) spectroscopy to identify changes of functional groups.
(iv) X-ray Photoelectron Spectroscopy (XPS) for identification of elements and their chemical state on the surface.
(v) Grazing Incidence X-ray Diffraction (GIXD) to identify beam-induced structural changes of the MP films.

2. Experimental

2.1. Target production

The targets were prepared from analytical grade lanthanide nitrates (Merck KGaA Darmstadt). The used solvents, isopropanol and isobutanol, and the nitric acid were also of analytical quality (Merck KGaA Darmstadt). The Ti backings had 99.9% purity (Goodfellow). A solution comprising a 9:1 ratio of isobutanol to isopropanol was employed for the deposition process. This ratio is the most commonly utilized solvent mixture for MP target production within our laboratory [28]. The lanthanides were then electrochemically deposited from this solution onto a 25 µm-thick Ti foil. The deposited area was circular with a diameter of 0.6 cm (area: 0.28 cm^2). The depositions were carried out galvanostatically at a constant current of 0.28 µA and for 1 h. The exact production method and the electrochemical cell construction are described in [28,31].

Table 1
List of studied samples and analytical methods applied. The uncertainty of the area density is assumed to be 10% based on an average of the density values given in the literature [32].

Sample name	Element	Area density $\frac{\mu g}{cm^2}$	SEM	Raman	IR	IBA	GIXD	XPS
Tb-50	Tb	50	x	x	–	–	–	–
Er-50	Er	50	x	x	–	–	–	–
Tm-50	Tm	50	x	x	–	–	–	–
Tm-500	Tm	500	–	x	x	–	x	x
Tm target-1	Tm	500	–	x	–	–	–	–
Tm target-2	Tm	500	–	x	–	x	–	–
Tm target-3	Tm	500	x	x	–	x	x	–
Tm target-4	Tm	500	x	x	–	x	x	–
Tm target-5	Tm	500	x	x	–	–	x	x
Tm target-6	Tm	500	–	x	x	–	–	x
HDZR-500	Tm	500	x	–	–	x	–	–

Table 2
List of irradiations. The first irradiation used 8.3 $\frac{MeV}{u}$ Au^{26+} ions at the M3 beamline of the GSI Darmstadt. For damage characterization of the Au-irradiated samples by means of ion beam analysis (IBA), we used a 1.2 $\frac{MeV}{u}$ Cl^{7+} beam at the HZDR. All samples have an area density of 500 $\frac{\mu g}{cm^2}$. The uncertainty of the area density and of ion irradiations are estimated to be 10%.

Sample name	Element	1st irradiation $\frac{Au\ ions}{cm^2}$	IBA	2nd irradiation $\frac{Cl\ ions}{cm^2}$
Tm target-1	Tm	3.0×10^{11}	–	–
Tm target-2	Tm	5.0×10^{11}	x	2.0×10^{14}
Tm target-3	Tm	1.0×10^{12}	x	2.4×10^{14}
Tm target-4	Tm	3.0×10^{12}	x	2.4×10^{14}
Tm target-5	Tm	5.0×10^{12}	–	–
Tm target-6	Tm	1.0×10^{13}	–	–
HDZR-500	Tm	–	x	8.7×10^{13}

2.2. Target irradiation

Irradiations were performed at the materials research beamline M3 at the UNILAC accelerator at the GSI Helmholtz Centre for Heavy Ion Research in Darmstadt, Germany, using 8.3 $\frac{MeV}{u}$ Au^{26+} ions. Homogeneous exposure of samples was achieved by using a slightly defocussed beam. To prevent heating of the samples, the ion flux was kept below approximately $2.0(2) \times 10^9$ $\frac{ions}{cm^2\ s}$. The applied fluence ranged from 3.0×10^{11} to 1.0×10^{13} $\frac{ions}{cm^2}$ with an estimated uncertainty of about 10%. This accumulated fluence corresponds to the first few minutes of the target irradiation in a superheavy element production campaign and thus provides insight on the effects during the target conditioning process.

The parameters for the irradiations with Cl and Au ions are given in Table 3 together with comparative data for Ca ion irradiations applied earlier during bake-in procedures [27]; because ^{48}Ca has been the most important projectile of the SHE research during the last decades [2]. For the density of the MP films, we presume 2.73 $\frac{g}{cm^3}$ [33] which is the density of a thulium carbonate and as such notably lower than that of thulium hydroxide and oxide.

The calculated ranges of the three different ion species exceed by far the thickness of 0.7 to 1.4 µm [29] or the achievable area density (about 500 $\frac{\mu g}{cm^2}$) of the MP films, as shown in Table 3. In contrast to typical SHE experiments [11,12], where the beam first penetrates the backing and then enters the target thin film, our samples were positioned with the thin film facing the ion beam. This was also considered

Table 3
Beam parameters for the different irradiations of Tm targets including the total kinetic energy in MeV per nucleon (MeV/u), the electronic and nuclear stopping power, the applied fluence as well as the projected ion range as calculated with the SRIM-2013.00 code, assuming a thulium carbonate target density of 2.73 g cm^{-3} [33]. The dose D is the product of the energy loss and the accumulated fluence.

Ion	Energy [$\frac{\text{MeV}}{\text{u}}$]	(dE/dx)e [$\frac{\text{keV}}{\text{nm}}$]	(dE/dx)n [$\frac{\text{keV}}{\text{nm}}$]	Fluence [$\frac{\text{ions}}{\text{cm}^2}$]	Range [µm]	Range [$\frac{\mu\text{g}}{\text{cm}^2}$]	Dose [MGy]
^{35}Cl	1.2	3.3	6.1×10^{-3}	20×10^{13}	16	4452	388.94
^{197}Au	8.3	17.9	2.2×10^{-2}	1×10^{13}	109	29 769	105.07
^{48}Ca	5.9	2.8	1.8×10^{-3}	7×10^{13}	85	23 160	106.50

in the calculations presented. The total absorbed dose in Gray was calculated by multiplying the electronic energy loss per unit pathlength (dE/dx)e with the fluence.

2.3. Target characterization

2.3.1. Scanning electron microscopy and energy dispersive X-ray spectroscopy

In order to evaluate the ion beam-induced surface modifications, scanning electron microscopy (Philips XL30) with an acceleration voltage of 20 kV was used. In some cases, the samples were sputter-coated by a thin silver layer to avoid charging effects during imaging. The elemental composition of the thin films was investigated by EDX and analyzed with the NIST DTSA-II Lorentz software package [34].

2.3.2. Elastic recoil detection analysis

Some of the Tm targets were analyzed with Elastic Recoil Detection Analysis (ERDA) at the Ion Beam Center of the Helmholtz-Zentrum Dresden-Rossendorf (HZDR) using a 1.2 $\frac{\text{MeV}}{\text{u}}$ Cl ion beam. The angle between the normal direction of the sample surface and the incoming beam was 75°, the scattering angle was 30°. The analyzed area was about 2 × 2 mm^2. The recoil atoms and scattered ions were detected with a Bragg Ionisation Chamber (BIC), which enables energy measurements and Z identification of the particles. H recoils were detected with a separate solid state detector at a scattering angle of 40°. The beam fluence is monitored using a gold plated rotating vane (1 Hz) and a solid state detector, which detects Cl backscattering from Au. This system is calibrated against the ion beam current measured with a Faraday cup. The resulting fluences per sample are given in Table 2.

2.3.3. µ-beam - spatially resolved RBS and PIXE

Some of the Tm targets were analyzed with RBS and PIXE at HZDR using a 3 MeV proton beam. The beam was focused to about 7 × 5 µm^2. The backscattered protons were detected at a scattering angle of 174° with a silicon strip detector. A Ketek silicon drift detector collimated to 80 mm^2 was used to detect the X-rays emitted from the sample. The detector was placed outside the sample chamber. In addition, a 65 µm aluminium absorber was used to further reduce the contribution of the X-rays from the Ti substrate and stop back-scattered protons from entering the detector. RBS was used to obtain depth profiles of the main elements except H, which cannot be detected by RBS. For C, N, and O evaluated cross-sections from SigmaCalc are used [35]. For Ti, there is no accurate data in the relevant energy range and for the used scattering angle. Therefore a measurement on the Ti backing foil was performed to obtain non-Rutherford cross-sections, which was possible using the program NDF [36]. AFM measurements across the pristine Ti foil showed a substantial roughness of rms = 39(8) nm. Thus the deduced cross-section might not be of universal validity.

In the case of the Tm thin films, a preliminary large-scale PIXE scan was conducted, after which individual areas of the thin film were selected for point measurements. All large PIXE scans contain 128 × 128 points or 128 × 100 points and have a size of 260 × 260 µm^2 or 260 × 205 µm^2, respectively.

2.3.4. Raman spectroscopy

Raman spectra from 50 cm^{-1} to 4000 cm^{-1} were collected with a Jobin Yvon (Horiba) LabRam HR 800 spectrometer equipped with an Olympus BX41 optical microscope and a Si-based charge-coupled device (CCD) detector. The instrumentation used a grating with 1800 $\frac{\text{grooves}}{\text{mm}}$ and a slit width of 100 mm. Excitation wavelengths of 633 nm and 488 nm were used. These parameters, and the optical path length of the spectrometer led to a spectral resolution of 0.8 cm^{-1}. The spectral acquisition time was set to 40 s for all measurements. In order to exclude modifications due to laser irradiation, long-term measurements were carried out analogous to [37]. The Raman spectra were assessed using the Fityk software [38].

2.3.5. Infrared spectroscopy

IR spectra were recorded with a Bruker Alpha Platinum-ATR. For this purpose, the Bruker Platinum ATR monolithic diamond crystal was pressed onto the MP thin films and the spectra were recorded in the Attenuated Total Reflection (ATR) setup. The IR spectra were recorded after all other analytical work was completed, as the ATR mode may mechanically damage the surfaces. The spectra were recorded using Bruker OPUS software and analyzed by the Spectragryph software package [39].

2.3.6. X-ray photoelectron spectroscopy

For elemental analysis, several selected samples were investigated by XPS, some time (days up to months) after their preparation. Irradiated samples were stored under ambient air for even longer times and underwent several other characterization methods beforehand. During the measuring campaign the samples were stored in a UHV-chamber (base pressure about 2.0×10^{-8} mbar) neighboring the XPS analysis chamber. The base pressure in the XPS chamber was kept below 5.0×10^{-10} mbar. XPS measurements were conducted using a monochromatic Al K_α ($\lambda = 8.3395$ Å) X-ray source and a hemispherical analyzer Phoibos 150 with HAS 3500 plus controller (all from Specs, Berlin). The microfocus high performance X-ray source XRC-1000 MF was equipped with a μ-FOCUS 500 monochromator (all from Specs, Berlin). XPS analysis and peak fitting were performed with CasaXPS [40] (Ver. 2.3.24 PR 1.0).

In general, charging effects result in a slight broadening of the Full Width Half Maximum (FWHM) and a shift of the XPS peaks. Such charge shifts can be corrected using a flood gun, which flushes the sample surface with low-energy electrons in order to compensate the charge. At the same time, the electron beam emitted by the flood gun can modify surface species [41,42]. Therefore, care has to be taken in the interpretation of the data.

2.3.7. Grazing incidence X-ray diffraction

In GIXD, a very small angle of incidence (ω) was chosen to limit the penetration depth of the photons to a thin surface layer of the film. The X-ray beam and sample were fixed to ensure a small angle of incidence ($\omega \approx 0.1$–5°) while the detector moves at an angle of 2Θ to collect diffraction signals. The structural information thus originates predominantly from the near-surface region (< 400 nm). For the GIXD measurements, a SmartLab device from the Rigaku company with a rotating anode was used with Cu K_α radiation ($\lambda = 1.5406$ Å).

3. Results and discussion

3.1. Morphology of MP films

3.1.1. Non-irradiated samples

The molecular plating method produces thin films with a characteristic morphology consisting of individual tiles separated from neighboring tiles by deep cracks down to the substrate as shown in a representative SEM image (Fig. 1 right). This morphology is extensively described for the MP process [43,44] and is also referred to as

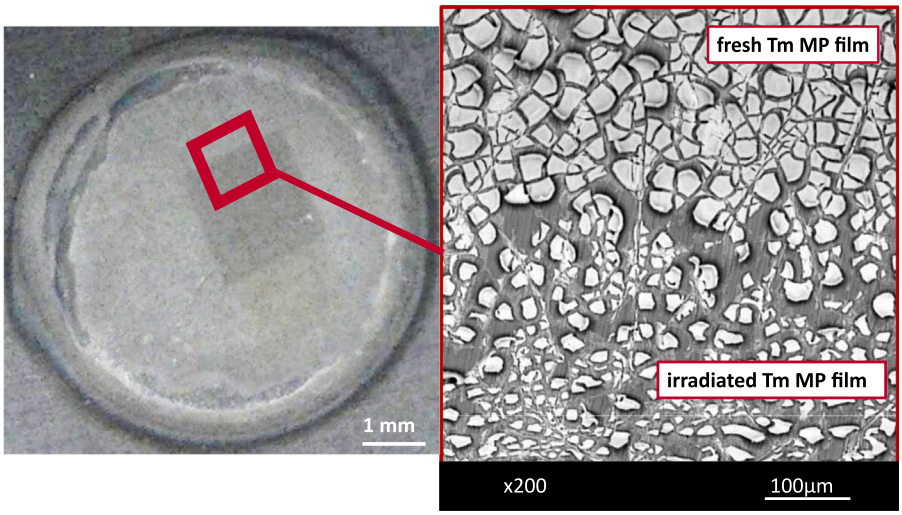

Fig. 1. Photograph (left) and SEM image (right) of a 500 $\frac{\mu g}{cm^2}$ thick Tm target (sample: HZDR-500) after irradiation with 1.2 $\frac{MeV}{u}$ Cl ions (2.0×10^{14} $\frac{ions}{cm^2}$). On the photograph, the irradiated area is clearly visible as dark square.

mudcracking [19,45] or mud-caking [46,47]. Each material produces a different mudcracking pattern and minute changes in MP parameters can have a large impact on the morphologies [43,48]. Other methods of electrochemical deposition of lanthanides and actinides also describe a cracked surface structure [45,49–51]. Vascon et al. showed that the cracks form after plating during drying and that the individual tiles of the thin film are not smooth, but have a rough substructure [48]. The formation of surface cracks depends mainly on the chosen solvent (isobutanol:isopropanol, 9:1). It should be noted that the solvent was kept constant throughout our experimental series.

Our scanning electron microscopy images clearly show (Fig. 1 right), that mudcracking leads to a significant portion of the surface of MP targets becoming uncovered. This effect should be taken into account during irradiation experiments and when utilizing analysis methods without a micrometre spatial resolution such as ERDA, GIXD and IR spectroscopy, etc.

3.1.2. Irradiated samples

First we discuss morphological changes of a fresh Tm MP film caused by the irradiation with 1.2 $\frac{MeV}{u}$ Cl ions (beam applied for ERDA). For an accumulated fluence of 2×10^{14} $\frac{ions}{cm^2}$, the changes in the irradiated area ($2 \times 2\,mm^2$) can easily be identified by the naked eye (Fig. 1 left). The sharp focus of the ion beam allows the interface between irradiated and non-irradiated area of the target to be displayed in one SEM image (Fig. 1 right) at high magnification. The SEM images of the two areas underline the difference; the characteristic tiles due to mudcracking are clearly visible in the non-irradiated area (Fig. 1 right). After the irradiation with 1.2 $\frac{MeV}{u}$ Cl ions, the tiles barely cover the Ti backing, they shrank in size and are strongly deformed (Fig. 1 right).

We also inspected the morphological changes of samples exposed to a fluence series with 8.3 $\frac{MeV}{u}$ Au^{26+} ions (Fig. 2, 1a–1c) and subsequently analyzed the films by ERDA with 1.2 $\frac{MeV}{u}$ Cl^{7+} ions (Fig. 2, 2a–2c). Up to the maximum applied Au ion fluence, the size of the tiles does not seem to change, but the uncovered area in between individual tiles becomes smaller. At the highest fluence (3.0×10^{12} $\frac{ions}{cm^2}$), Tm covers the Ti backing almost without cracks. Comparable observations have been described for MP gadolinium films [29].

Samples that were irradiated with Au ions and then ERDA-analyzed with the high-intensity Cl beam are shown in Fig. 2, 2a–2c. Morphological changes were also observed in samples irradiated with Cl ions only. Individual tiles exhibit deformation and shrinkage, but the overall effects appeared to be less pronounced the larger the fluence of the preceding Au irradiation.

3.2. Ion beam analysis

Damage effects in samples exposed to 1.2 $\frac{MeV}{u}$ Cl ions for ERDA were analyzed with a μ-beam RBS/PIXE. The border area between ERDA-irradiated and non-irradiated sample surface was examined, so that the influence of irradiation on the thin films could be studied (Fig. 4a). A sketch (Fig. 3) of the cross-section of the non-irradiated MP thin films, as derived from our microscopy images and the existing literature [31,52,53], illustrates the challenges in the application of ion beam methods in materials analysis.

3.2.1. Non-irradiated samples

The analysis of RBS and PIXE with a μ-beam made it possible to spectroscopically investigate individual tiles on the mudcracked surface. The element concentrations calculated from the RBS depth profiles for individual tiles of non-irradiated MP thin film (thickness 500 $\frac{\mu g}{cm^2}$) are dominated by the elements C and O (Fig. 4c). Tm is only a minor component in atomic percent of the thin films. The *N* signal is characterized by a poor signal-to-noise ratio, which is why nitrogen is just barely detectable by RBS. Still, the weakness of the *N* signal suggests that we can exclude a significant deposition of nitrate species, which is consistent with other spectroscopic studies [48,52]. The Ti signal from the backing foil varies between individual tiles, which indicates that the tiles are of different thicknesses. The signal strength remained consistent across all tiles for the other elements. The depth profiles are obtained after analysis using the NDF-code [36] and conversion from the spectrum recorded during the RBS measurement. The film thicknesses obtained from the analysis are given in units of at/cm^2. A conversion into a length unit is problematic as the mass density of the film is not precisely known. A length estimate based on the weighted average of the atomic densities gives a film thickness of about 2 µm for the μ-beam measurements (Fig. 4 (c,d)), which is consistent with our AFM and 3D laser scanning microscope measurements (not shown).

3.2.2. Irradiated samples

Comparing the PIXE data at the transition between non-irradiated and irradiated thin film (Fig. 4b), we first see that the elemental distribution of the PIXE map reproduces quite well the morphology of the MP thin films, as observed by SEM (Fig. 1 right). The higher intensity of the Tm-L signal is the result of Tm being accumulated in a smaller area. Furthermore, the distances between the Tm island or MP tiles are larger than in the non-irradiated area.

The RBS element analysis of the non-irradiated area (Fig. 4c) is dominated by C and O. Irradiation leads to the loss of most of the

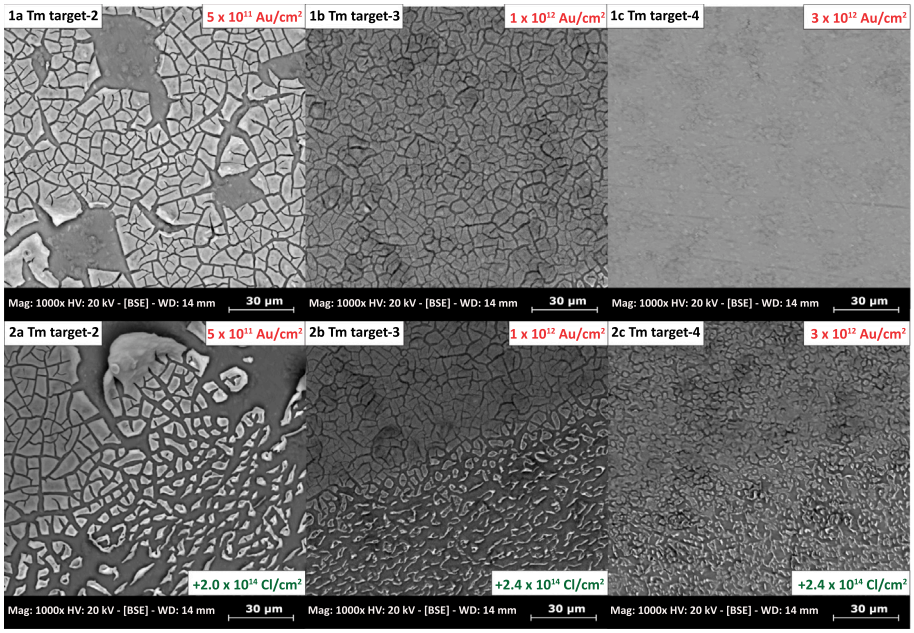

Fig. 2. SEM images of MP Tm thin films (thickness 500 $\frac{\mu g}{cm^2}$, samples: Tm target-2 to Tm target-4) irradiated with different fluences. Top row (1a-1c): Tm films irradiated with 8.3 $\frac{MeV}{u}$ Au ions at increasing fluence. Bottom row (2a-2c): same sample series after ERDA analysis using 1.2 $\frac{MeV}{u}$ Cl ions of fluence 2.0×10^{14} $\frac{ions}{cm^2}$ to 2.4×10^{14} $\frac{ions}{cm^2}$. The lower series shows exactly the transition area of the ERDA analysis beam spot. Note that the SEM image 1c is slightly defocused, making the surface appear smoother than it really is.

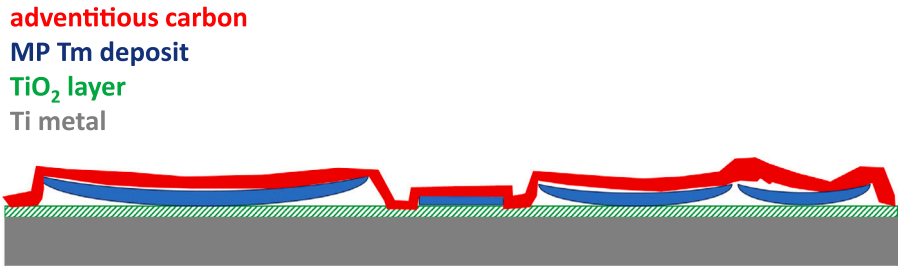

Fig. 3. Sketch of cross-section through the MP Tm film, to illustrate the difficulties of XPS, RBS and ERDA measurements due to tile formation, cracks and adventitious carbon contamination.

carbon. Due to the irradiation, the relative proportion of Tm increases, oxygen and Tm become the dominant components, C is detectable just above the measurement background and nitrogen is below the detection limit (Fig. 4d).

The ERDA investigation of the fluence series of Au-ion irradiated Tm samples (Fig. 5) confirms the decrease of the overall carbon and oxygen concentration as a function of fluence. The depth profile of the oxygen concentration fits well with the oxygen contents that were detected in the irradiated thin films by means of RBS. The carbon content determined by ERDA is higher than what was determined by the RBS measurements of irradiated thin films. The irradiation-induced alterations of the thin films, namely compaction and the loss of light elements, rendered the evaluation of the ERDA data a challenging endeavour. The ERDA measurements were further complicated by the morphology of the samples, a problem that is circumvented in RBS/PIXE measurements due to their superior spatial resolution. Collectively, the ERDA measurements align with the hypothesis that the irradiation with energetic heavy ions results in a depletion of C and O in MP thin films. Based on the results obtained from the ion beam methods, no significant beam-induced loss of Tm was observed. Instead, the combined PIXE/RBS/ERDA data suggest that the MP film tiles lose volatile components containing O and C, as a consequence of irradiation. This may result in chemical transformations that could potentially lead to the formation of a compound with a higher density, which in turn would result in a reduction of the area covered by the MP thin film.

We conclude from our data, that the determination of the elemental composition by the applied ion beam analysis was clearly at the limit of statistical significance for both non-irradiated and irradiated thin films. Techniques with high spatial resolution (e.g. using a μ-beam) are particularly suitable for overcoming challenges associated with the morphology of the MP films.

3.3. Vibrational spectroscopy

3.3.1. Non-irradiated samples

After achieving promising results using confocal Raman spectroscopy on lead model systems [26,27], we applied the method on a series of thin MP-produced lanthanide films including Tb, Er, and Tm (Fig. 6). The exceptional spatial resolution of this method enabled us to spectroscopically examine individual tiles, ensuring that the complex morphology and the presence of a Ti backing did not affect the accuracy of the measurements. Despite the thin Tb films exhibiting more pronounced mudcracking compared to Er and Tm, their Raman spectra are remarkably similar (Fig. 6). Furthermore, none of the samples exhibit any orientation-dependent behavior in their Raman spectra, indicating that they are in an amorphous or microcrystalline state composed of randomly oriented microcrystals [54].

The Raman spectra were recorded by means of the confocal Raman microscope using two different lasers with wavelengths, 473 nm and 633 nm, of the confocal Raman microscope. Several different tiles were

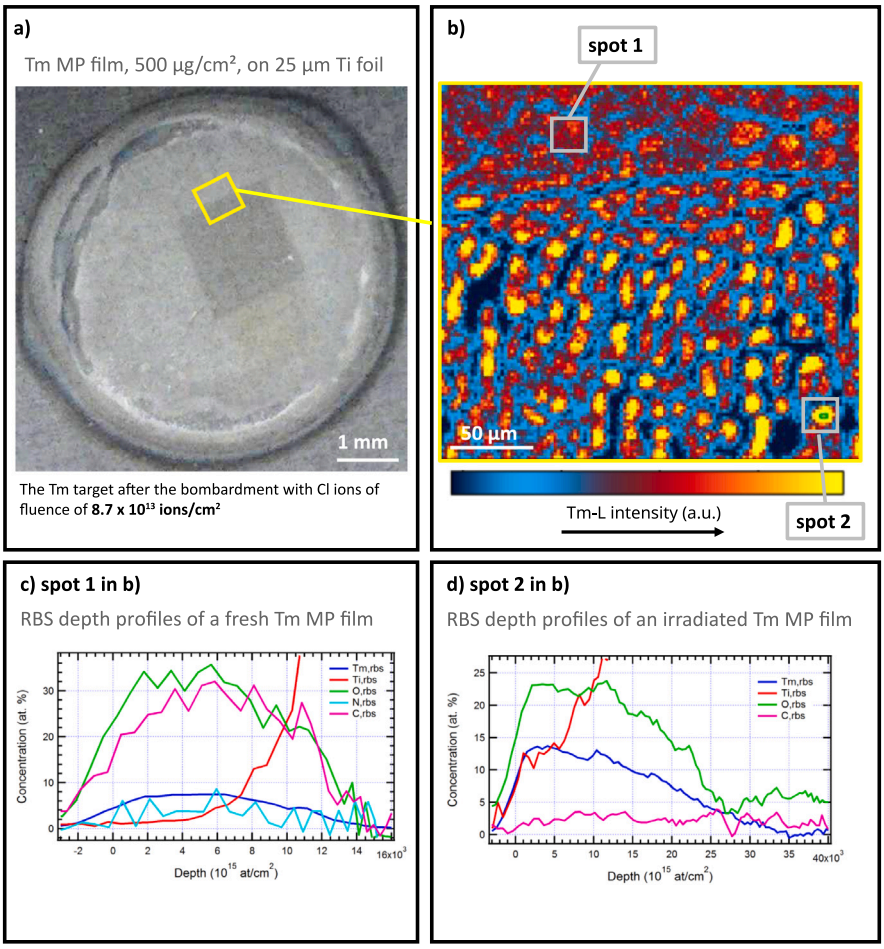

Fig. 4. (a) Photograph of MP Tm thin film (sample: HZDR-500) with yellow frame indicating the PIXE analyzed area performed after ERDA analysis with 8.7×10^{13} $\frac{\text{ions}}{\text{cm}^2}$ of 1.2 $\frac{\text{MeV}}{\text{u}}$ Cl ions. (b) PIXE map of non-irradiated (top area) and Cl-ion exposed area (bottom). The color code corresponds to high (yellow) and low (blue) Tm concentrations. Spot 1 and 2 indicate spots analyzed by μ-beam RBS analysis. (c) and (d) RBS data for various elements from spot 1 (non-irradiated) and spot 2 (Cl ion irradiated), respectively.

examined per sample in order to produce representative results for each sample. The spectra were identical for both excitation wavelengths and exhibited identical peak intensities. The ratio of the peak positions also remained constant, but the peak positions themselves fluctuated by about 3 cm^{-1} from measuring point to measuring point. According to [52], MP films are armorphous material, while the reference literature cited below refers exclusively to monocrystalline materials. For the final fit of the bands and the assignment to literature values, the spectrum with the lowest background was selected (Fig. 7).

In the Raman spectra of our Tb, Er and Tm films, carbonate [54–57] and formate [58–60] could be identified. Some Raman modes of the chemically closely-related anions overlap (Fig. 7). The identified bands are given in Table 4 and assigned to Raman modes where possible. Herzberg [61] nomenclature was used.

The wavenumber range from 50 to 700 cm^{-1} is characterized by a high background and a poor signal-to-noise ratio. We thus ignored this wave number regime for the analysis (Fig. 6). At larger wavenumbers, the spectrum is dominated by two bands, a sharp narrow peak (902 cm^{-1}), which can be assigned to the out-of-plane bend (ν_2) of the carbonate ion, as well as a multiplet (2733 to 3066 cm^{-1}), which is assigned to the C–H stretching vibration of the formate. Most of the other peaks in the spectrum can be assigned to either anion.

The free carbonate anion belongs to the point group D_{3h} and therefore has four vibrational transitions [55]. We assign the bands between 1560 to 600 cm^{-1} (Table 4) to coordinated carbonate. The four normal vibrational transitions are expected in a range from 1090 to 1070 cm^{-1} (ν_1), 930 to 850 cm^{-1} (ν_2), 1560 to 1420 cm^{-1} (ν_3) and 820 to 750 cm^{-1} (ν_4). The splitting of the degenerate modes ν_3 and ν_4 may be caused by the symmetry reduction from D_{3h} to C_{2v} or C_s from the free to the coordinated carbonate anion [57]. In an amorphous phase all four vibrational transitions of the carbonate ions are expected to be both infrared and Raman active. Furthermore, one would expect that the degeneracy of the ν_3 and ν_4 modes for the free carbonate ions is lifted [55]. Detailed correlation schemes and group theory discussion of the spectroscopy of carbonate in solid phases can be found in [55–57]. The observed Raman spectra (Fig. 7) can therefore be partly explained by bound carbonate in an amorphous phase.

The free formate anion has the point group C_{2v}, thus six vibrational transitions can be derived from group theory [58–60]: The C–H stretch in the range from 3070 to 2730 cm^{-1} (ν_1), the O–C–O symmetric stretch from 1380 to 1360 cm^{-1} (ν_2), the O–C–O symmetric deformation from 820 to 750 cm^{-1} (ν_3), the O–C–O asymmetric stretch from 1610 to 1580 cm^{-1} (ν_4), the C–H in-plane bend from 1430 to 1420 cm^{-1} (ν_5) and the out-of-plane bend from 1080 to 1005 cm^{-1} (ν_6) [60]. Only the most intense bands at 2918 cm^{-1} and 2942 cm^{-1} can be unambiguously assigned to the C–H stretch (ν_1) of the formate [59], which is in good agreement with the reported literature values of 2920 cm^{-1} and 2949 cm^{-1} [58]. For the other transitions, no exactly measured or calculated values are given for thulium formates, but they are available for homologues from the lanthanide series. As in the case of carbonate, symmetry reduction in amorphous materials would be an explanation for the occurrence of bands that are in principle symmetry-forbidden bands in the Raman spectrum. The C–H stretching vibration (ν_1) is of particular importance in formates, thus its variation within the lanthanide series has been systematically studied [58,60].

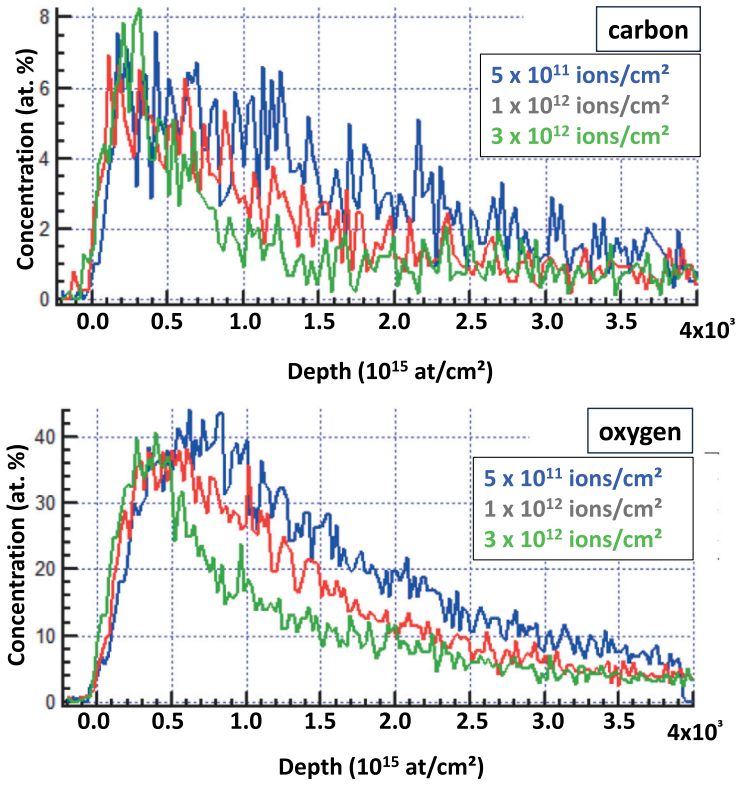

Fig. 5. C and O concentration as a function of depth deduced from ERDA spectra for MP Tm thin films (sample series Tm target-2 to Tm target-4). The contribution of both elements decreases with depth and with increasing fluence.

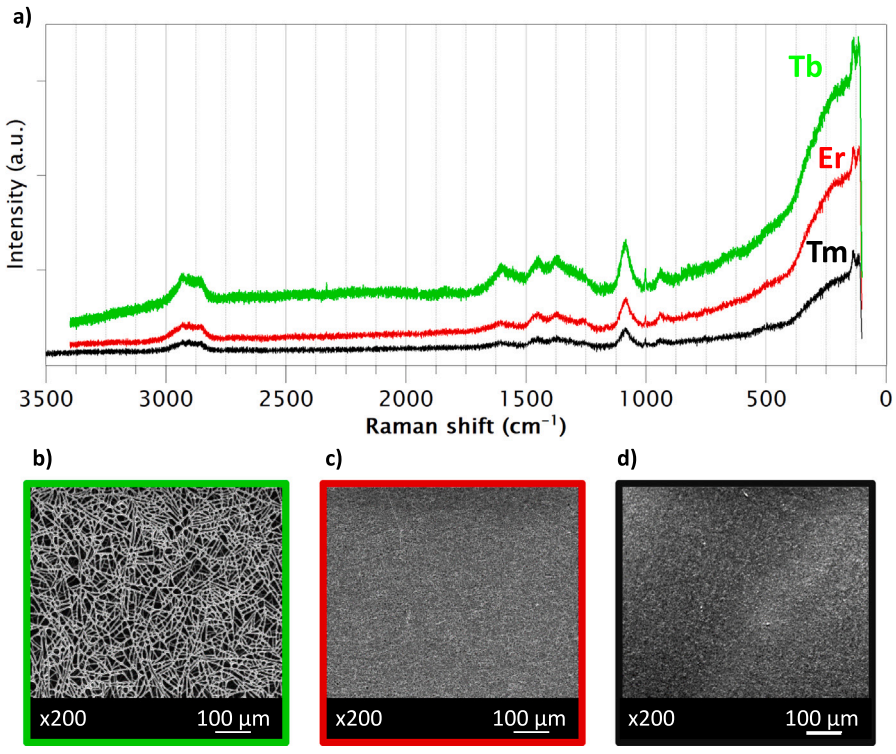

Fig. 6. (a) Raman spectra of Tb (sample Tb-50), Er (sample Er-50) and Tm (sample Tm-50) films of thickness: 50 $\frac{\mu g}{cm^2}$ and (b)–(d) respective SEM images. Despite different morphologies, MP thin films of different lanthanides show the same Raman spectrum.

It should be mentioned that the nitrate anion also has a D_{3h} symmetry and should thus produce Raman bands similar to those of carbonates, which is how Raman spectra of uranium MP films were interpreted [63]. However, due to the very different chemistry of uranium compared to lanthanides and heavy actinides, this interpretation of the Raman spectra cannot be applied. Other studies on uranium

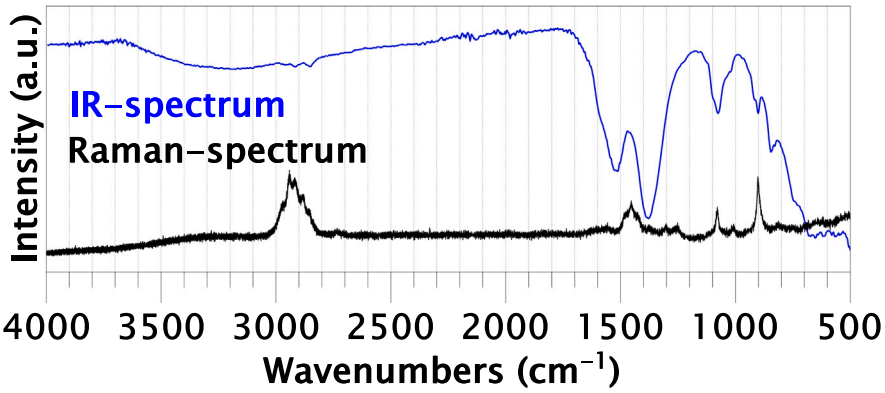

Fig. 7. Raman and IR spectrum of MP Tm thin film (thickness 500 $\frac{\mu g}{cm^2}$, sample: Tm-500).

Table 4
Assignment of bands in the Raman and IR spectra of the non-irradiated MP Tm films, as designated by Herzberg [61].

Wavenumber	Method	Carbonate	Formate	References
401	IR	Unknown		
563	IR	Unknown		
619	IR	ν_{4a}	–	[62]
653	IR	ν_{4b}	–	[62]
673	IR	ν_{4c}	–	[62]
754	Raman	ν_{4a}	ν_{3a}	[55–58,60]
813	Raman	ν_{4b}	ν_{3b}	[55–58,60]
846	IR	ν_{2a}	–	[62]
901	IR	ν_{2b}	–	[62]
902	Raman	ν_2	–	[55–57]
1008	Raman	–	ν_{6a}	[60]
1076	IR	ν_1	–	[55–57]
1079	Raman	ν_1	ν_{6b}	[55–57,60]
1252	Raman	Unknown		
1302	Raman	Unknown		
1374	Raman	–	ν_{2a}	[58,60]
1379	IR	ν_{3a}	ν_{2a}	[58,60,62]
1423	Raman	ν_{3a}	ν_{5a}	[55–58,60]
1453	Raman	ν_{3b}	–	[55–57]
1476	Raman	ν_{3c}	–	[55–57]
1514	IR	ν_{3b}	–	[62]
1557	Raman	ν_{3d}	–	[55–57]
1583	Raman	–	ν_{4a}	[59,60]
1605	Raman	–	ν_{4b}	[59,60]
2733	Raman	–	ν_{1a}	[58–60]
2770	Raman	–	ν_{1b}	[58–60]
2882	Raman	–	ν_{1c}	[58–60]
2915	IR	–	ν_{4a}	[58]
2918	Raman	–	ν_{1d}	[58–60]
2942	Raman	–	ν_{1e}	[58–60]
2960	IR	–	ν_{4b}	[58]
3066	Raman	–	ν_{1f}	[58–60]

MP targets could not detect any nitrate in the thin films by Raman and IR [64] or XPS [65,66], and the thin films were reported to be nitrogen-free.

3.3.2. Irradiated samples

Fig. 8 shows spectra from a series of 8.3 $\frac{MeV}{u}$ Au ion irradiations. With increasing fluence, the two most prominent Raman bands (at 1079 cm^{-1}(a) and at 2942 cm^{-1} (c)) disappear and two new bands (b) gradually emerge around 1590 cm^{-1} (1650 to 1480 cm^{-1}) and 1360 cm^{-1} (1440 to 1290 cm^{-1}).

The two new bands can be assigned to the D (1440 to 1290 cm^{-1}) and G (1650 to 1480 cm^{-1}) peaks, which are characteristic for graphite-like structures embedded into an oxide structure [67–69]. The G-band is the primary mode in graphene and graphite. It represents the planar configuration sp^2-bonded carbon that constitutes graphene. The band is resonant, which means that it is much more intense than would be expected otherwise. The D-band is known as the disorder band or the defect band. It represents a ring breathing mode from sp^2 carbon rings, though to be active the ring must be adjacent to a graphene edge or a defect. A significant D-band indicates defects to be present in the material. The intensity of the D-band is directly proportional to the level of defects in the sample [70]. In light of the aforementioned findings, it can be posited that the irradiated MP thin films can be characterized as amorphous oxides with embedded carbon clusters, as evidenced by the results of our Raman spectroscopy analysis [69].

The IR spectrum of the sample with the highest fluence is plotted together with the Raman spectrum of the same sample in Fig. 9. In the region of high wavenumbers, there is also IR activity that could be assigned to OH-oscillations. The hygroscopicity of the samples may be a potential explanation for the origin of these OH-oscillations. Otherwise, the IR spectrum of the irradiated samples does not permit further identification of chemical species. Yet, the appearance of oxycarbonates has been inferred from earlier GIXD and XPS studies [52], for lanthanum MP thin films that were heated to 700 K. However, Raman and IR spectra of these oxycarbonates [71] could not be identified in our films. Therefore, ion irradiation obviously induces a different form of transformation rather than pure heating [29].

3.4. X-ray photoelectron spectroscopy (XPS)

In the XPS overview spectra (not shown) of the MP Tm thin films the expected characteristic Tm, O, and C peaks as well as the peaks of Ti are visible. The Ti signal originates from the Ti backing due to the mudcracking morphology as illustrated in Figs. 1 and 3. The tiles do not completely cover the surface and therefore, the Ti backing (together with its oxide layer) is exposed to the analyzing X-ray beam.

The electrical conductivity of the MP films is rather poor, which favors charging effects [72,73] during the XPS measurement. As is typical for air-exposed samples, they are covered with so-called “adventitious carbon”, a layer of short-chain oxygen-containing organic carbon compounds. Together with charging effects, this makes the direct interpretation of the C1s spectra difficult [41,74]. Further, it is important to note that numerous authors report charge-corrected measured binding energies. Often, the dominant C1s peak is attributed to adventitious carbon and placed in a range of 284.5 to 285.5 eV. This approach leads to inconsistencies in the energy positions among different reports as the final charge-corrected binding energy is not necessarily accounting for the nature of different organic species [41,74]. Therefore in this experimental series we tried to avoid relying on the absolute, charge-corrected BE values, but rather used peak differences instead for our interpretations [42].

Despite the problems described in the previous paragraphs, we discuss in the following the change in C1s spectra under irradiation. The C1s region (Fig. 10) for the irradiated samples is less complex than that of the fresh MP samples. The number of carbon species needed

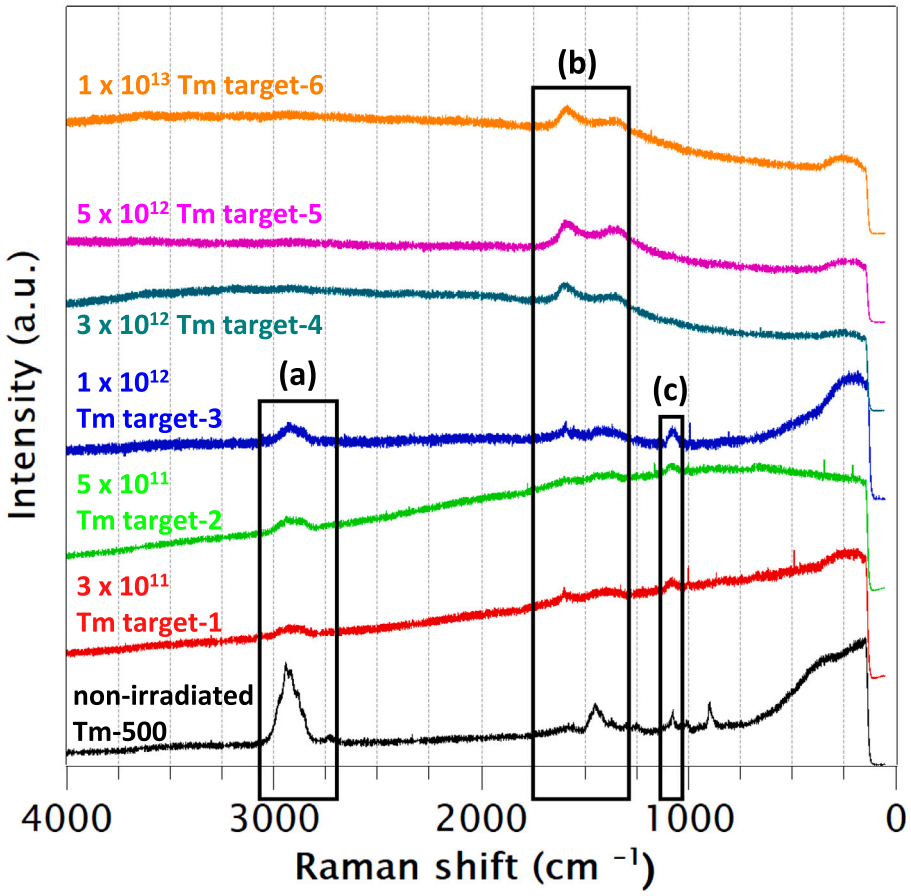

Fig. 8. Raman spectra of a Tm sample series (Table 2) irradiated with 8.3 $\frac{\text{MeV}}{\text{u}}$ Au ions of different fluences. The boxes indicate the position of bands assigned to formate (a), graphite (D and G band) (b) and carbonate (c). The fluence is given in units of $\frac{\text{ions}}{\text{cm}^2}$.

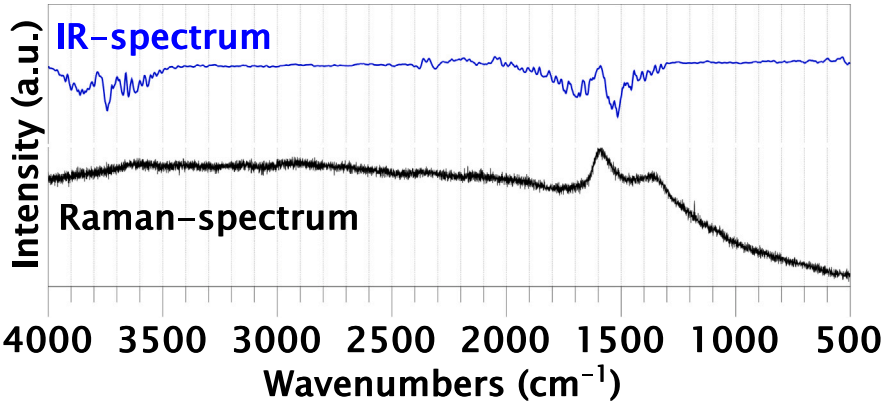

Fig. 9. IR and Raman spectra of MP Tm thin film (thickness 500 $\frac{\mu\text{g}}{\text{cm}^2}$, sample: Tm target-6) after irradiation with 8.3 $\frac{\text{MeV}}{\text{u}}$ Au ions of fluence 10^{13} $\frac{\text{ions}}{\text{cm}^2}$.

to develop a peak model is reduced for the irradiated samples and the peak observed above 292 eV is absent after irradiation. Table 5 summarizes the assigned chemical species. Carbon species containing C–Cl and C-N bonds were excluded from consideration as no indications for the presence of Cl and N were obtained in XPS overview spectra, nor with other analytical methods like RBS or ERDA. Fluorine was observed only for the irradiated films (samples Tm target-5 and Tm target-6) and is assumed to be due to surface contamination during sample handling or storage in an UHV-chamber. We ascribe the peaks in the C1s XPS spectra to the following three carbon species: (i) a thin layer of adventitious carbon-containing material on the conductive Ti [74], (ii) the same layer on the MP thin film and (iii) the confirmed carbon species in the MP thin film itself.

The C1 peak is interpreted to represent the C–C/C–H contribution of the adventitious carbon on the Ti backing (Fig. 10). This is supported by the absence of the peak when no Ti is detected in overviews and Ti2p detail spectra. The Binding Energy (BE) corresponds to the value measured on a blank Ti reference backing (not shown) without deposited film. The superposition of the peaks in the irradiated samples (Fig. 10b and 10c) illustrates a major problem of interpretation. The main peak can be fitted with variable proportions of adventitious carbon contributions, i.e. both C1 and C2 species in variable proportions. This discrepancy is likely due to the challenging morphology of the samples,

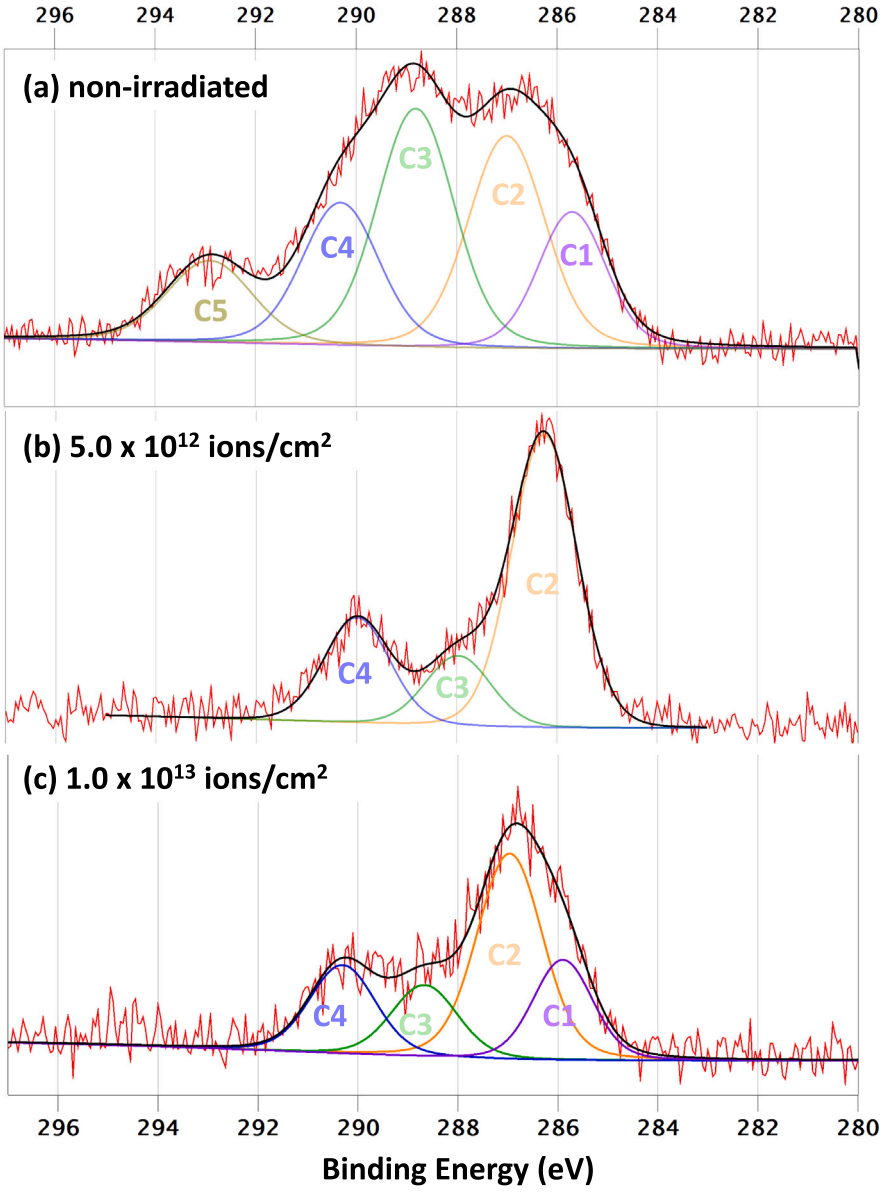

Fig. 10. C1s XPS spectra of MP Tm samples together with fits of individual carbon species for non-irradiated sample (top) and two samples irradiated with 8.3 $\frac{\text{MeV}}{\text{u}}$ Au ions of different fluence. The samples shown are Tm-500 (a), Tm target-5 (b) and Tm target-6 (b).

Table 5
Measured Binding Energy (BE) and Chemical Shift (CS) of different carbon species.

Peak	BE eV	CS eV	Possible species
C1	285.7		C–C/C–H contrib. of advent. carbon on Ti backing [74]
C2	286.3–287.0		C–C/C–H contrib. of advent. carbon on MP Tm film [74]
C3	287.9–288.8	1.5–1.8	C–O–C, C–OH, C*–O–C=O [40]
C4	290.0–290.4	3.3–3.7	C–O–C*=O HCOO [40]
C5	292.8–292.9	5.9	O=C(–O–)2 [40]

in addition to the limitations of the XPS method, such as charging effects.

Given the intricate surface morphology of the samples and the ion-beam-induced inconsistency in the XPS spectra, a quantification of the Tm-C ratio was deemed to be unreliable and unsound. Additionally, the issue of adventitious carbon (Table 5) on the Ti backing alone would have rendered further calculations even more arbitrary.

However, the clear change in the C1s spectra induced by the ion irradiation can be reconciled with the results of Raman spectroscopy and ion beam analysis, which suggest that the freshly deposited formates, (hydroxo)carbonates, hydroxides change under irradiation to a more oxidic species with intercalated carbon clusters.

Also in the O1s region distinct differences between the freshly deposited and the irradiated samples are observed (Fig. 11a). Again, a BE component at 532 eV is observed that correlates with the presence of Ti in the spectra. This is likely due to an oxidized Ti surface (TiO_2). For the blank Ti reference sample, an oxidized layer was observed as well. Another assignment possibility would be a thulium oxide component [75]. In a freely accessible database for XPS spectra, Tm_2O_3 is characterized by a double peak, the peak energy is given as 532 eV.

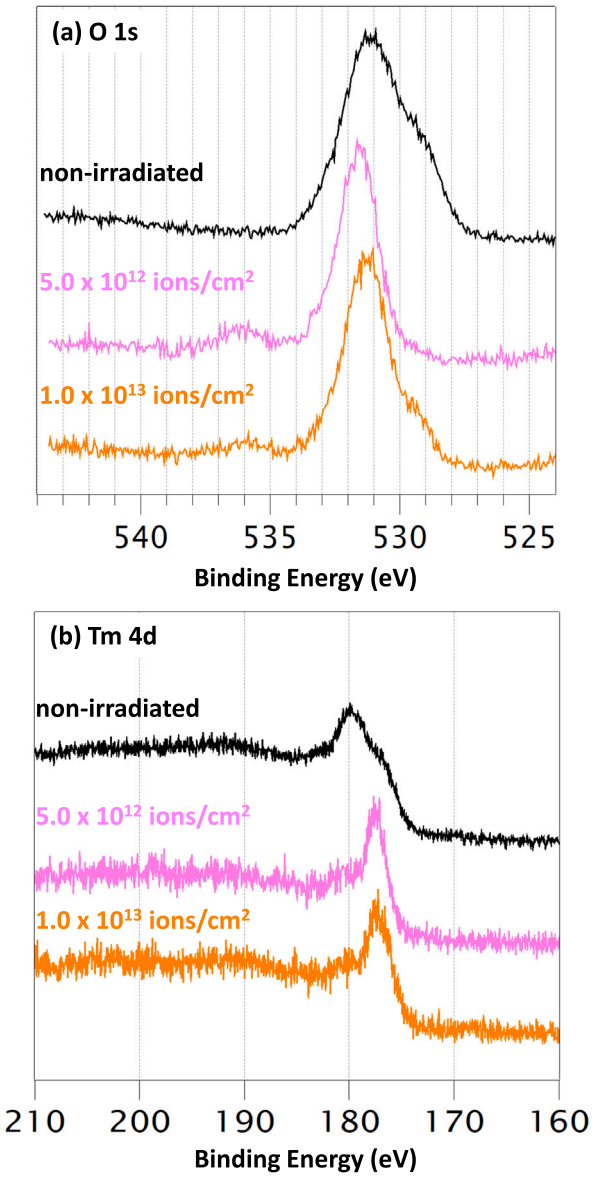

Fig. 11. (a) O1s and (b) Tm4d XPS spectra of MP Tm samples for a non-irradiated sample (top) and two samples irradiated with 8.3 $\frac{\text{MeV}}{\text{u}}$ Au ions of different fluence. The samples shown are Tm-500 (black), Tm target-5 (pink) and Tm target-6 (orange).

In principle, the O1s peaks of metal oxides are characterized by a narrow peak shape, while the peaks of carbonates or formates should be broader. The shoulder at 529 eV in the non-irradiated samples could be explained by carbonate or formate based on the other analysis results, but this is not certain due to the inconclusive energy calibration. Furthermore, metal carbonates would be expected at higher, not lower BE than metal oxides [53]. Thus, no clear, unambiguous conclusion can be drawn from the O1s spectra alone.

In the Tm4d region differences are observed between non-irradiated and irradiated samples (Fig. 11b). While the fresh samples display a double peak structure for the 4d maximum, this is not distinctly seen for the irradiated samples. The double-peak structure in the Tm4d spectrum of the non-irradiated MP samples may be due to a differential charge shift effect that is not fully compensated by the flood gun, the intrinsic shape of the deposited material, or a superposition of different chemical species.

3.5. X-ray diffraction

For structural analysis of our thin films, X-ray diffraction under grazing incidence was performed (Fig. 12). Non-irradiated MP thin films yield only three broad and weak reflections, which can be best fitted with thulium formate [58,76,77]. Based on the half-width of the reflexes, the size of the crystallites in the sample that contribute to the reflex can be deduced. The diffraction pattern of our samples is thus indicative of the amorphicity of the phases and is consistent with the literature for diffraction experiments on untreated lanthanum MP films on Ti foils [52]. The roughness of the Ti substrate [78,79] used also made the diffraction measurements more difficult and certainly contributes to the dominance of the Ti reflections. The characterization of irradiated MP films was unsuccessful. This is attributed to the further amorphization. Yet, future diffraction experiments with even smaller angles of incidence together with Synchrotron X-ray Diffraction (SXRD) could enable a reliable identification of the different crystallites in the MP thin films.

4. Summary

4.1. Characterization of fresh films prepared by molecular plating

Microscopic methods confirm that of thin Tm films produced by molecular plating on a Ti backing are fractured, exhibiting a mudcracking morphology (Fig. 1 right). The films are composed of individual tiles, which significantly impacts the applicability of various analysis methods (Fig. 3). The most accurate results were obtained using high spatial resolution analytical methods such as Raman and RBS/PIXE, which allowed us to analyze individual tiles.

Our XPS characterization showed that the fresh films do not contain significant amounts of N, although Tm was added as nitrates in diluted nitric acid in the MP process. This result for *N* agrees well with the literature for the MP process from alcoholic solvents [48,52]. Studies on the MP process with aqueous nitrates from DMF [80] also showed no significant *N* in the XPS spectra, which in this particular case, also excludes the intercalation of nitrogen-based solvent degradation products. Thus, nitrogen compounds, such as nitrates and their degradation products, can be excluded as a constituent component of MP thin films.

The C1s XPS spectra of non-irradiated MP films showed a whole range of different carbon species. Unambiguous chemical identification by XPS alone is not possible, but in accordance with literature [48, 52,80] the assignment of the dominant carbon compounds in the MP thin film to the carbonates and a carboxylic acid-like species (Table 5) is apparent. The formation of carbonates right after electroplating can be excluded, because the phase diagrams in the literature [81] clearly show that at room temperature and under ambient concentration of carbon dioxide (about 600 ppm) in the laboratory air, the formation of lanthanide carbonates is negligible [82,83]. Therefore, it can be concluded that the formation of carbonates through the weathering of hydroxides and oxides is an unlikely mechanism. A similar behavior is to be expected for the production process of heavy actinide targets, but literature data are scarce. Experiments reported in [31,48] clearly showed that the C1s species are formed during the MP process and not by drying the thin films in laboratory air. In addition, several XPS studies [48,65,80] have demonstrated that the carbon species in MP thin films is not a surface phenomenon, but is intrinsic to the entire thin film.

The XPS oxygen spectra did not permit a clear identification of the chemical species of the MP thin films and could not be reconciled with the assignments of the C peaks. This is because different binding energies would be expected for carbonates or carboxylic acid-like species, but from our XPS analysis, which is afflicted by differential charging, a reliable determination of binding energies is not possible. Publications on XPS studies of MP thin films often neglect discussion of the oxygen spectra. However, in one XPS study [80] on samarium MP films, the

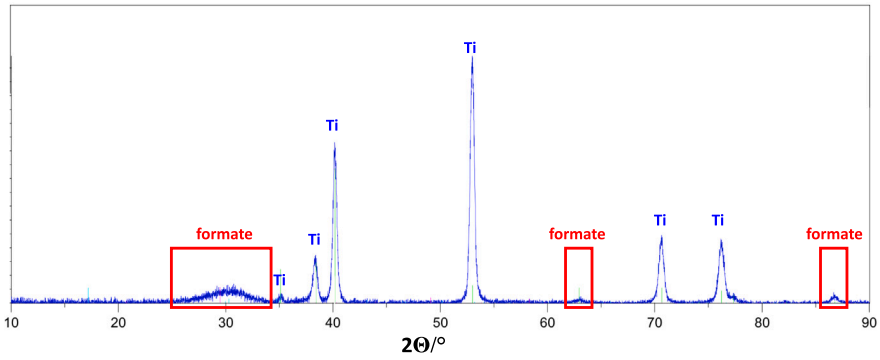

Fig. 12. GIXD diffractogram of non-irradiated MP Tm sample (sample: Tm-500), the red boxes show the reflections that can be assigned to thulium formate, while the sharp reflections originate from the Ti backing.

O1s spectra were discussed, and the observed O1s binding energy could be attributed to carbonates based on the observed C1s spectra.

Our ion beam analysis experiments also showed that C and O are the dominant species in fresh MP thin films. In both the ERDA (Fig. 5) and RBS (Fig. 4c and 4d) depth profiles, O and C dominate over the intended lanthanides in atomic percent. Again, a conclusive quantification of the MP film constituents was not possible, i.e., no sum formula of the MP thin films could be determined.

From GIXD measurements, we conclude that the MP films are amorphous and that Tm exists in the formate phase (Fig. 12). Due to the amorphous structure [52] of the MP thin films, as well as the roughness of the Ti backings, the results are not very clear. Moreover, the challenging morphology makes it difficult to interpret the GIXD data. By means of vibrational spectroscopy, carbonates and formates were identified as components of the fresh films (Fig. 7).

4.2. Chemical changes induced by heavy-ion irradiation

The irradiation of Tm MP thin films with 8.3 $\frac{\text{MeV}}{\text{u}}$ Au ions induces drastic changes in morphology (Fig. 2). With increasing fluence, the cracks disappear and Tm becomes more and more homogeneously distributed across the entire surface. This effect has also been reported for MP plated Gd films [29]. Upon further irradiation with Cl ions of 1.2 $\frac{\text{MeV}}{\text{u}}$, (characterized by a lower energy loss than the 8.3 $\frac{\text{MeV}}{\text{u}}$ Au ions), films pre-irradiated with Au ions exhibit fewer morphological changes than non-irradiated films (Fig. 2).

Analysis by RBS revealed that the ion irradiation drastically reduces the C content of the MP thin films (Fig. 4). The RBS spectra of the irradiated films are dominated by O and Tm. Overall, the relative proportion of the target element is larger after irradiation, probably because a large fraction of volatile by-products from the MP process outgassed. This loss of unwanted material through the first irradiation could be an explanation for the beneficial effect of the conditioning process [20,21]. Our ERDA investigation showed that the loss of O and C increases with fluence (Fig. 5).

The XPS measurements of the irradiated MP films underline beam-effects on the C component (Fig. 10). No clear chemical species can be assigned. However, within the C1s peak, the loss of carbon species with higher binding energies, e.g. carbonates and formates, is obvious. The carbon species (Table 5) with the highest relative binding energy (C5, carbonate-like) disappears completely through irradiation. In contrast, an aliphatic carbon species (C2) is the dominant component of the MP thin films following irradiation. We were not able to identify by XPS compounds with higher binding energies as seen by Raman spectroscopy. Our XPS data clearly demonstrate the loss of carbon species and the disappearance of carbonates.

IR and Raman spectroscopy (Fig. 9) provide evidence for newly formed chemical species. Two characteristic Raman bands are visible over a very high background, which fit an assignment to C nanoparticles [67,69]. In the IR spectra hydroxide bands were identified. Based on the overall spectroscopic findings, the irradiated MP thin films can be best described as amorphous oxide with embedded C nanoparticles.

5. Conclusion

The established models for the MP process assumed the formation of hydroxyl ions during deposition according to Hansen's theory [84–87]. Due to the non-reduction of the lanthanide or actinide cations [48,52, 65,80], basic precipitation is assumed to occur by a combination of electrophoresis and electroplating [43]. The observed C content was explained by intercalated solvents and products of solvent decomposition. The analytical methods used in this study could not detect any decomposition products from the solvents used. The origin of observed C content is not clear, but organic solvents can dissolve much more carbon dioxide than, e.g., water can. At room temperature and normal pressure, the solubility of carbon dioxide in water is 0.033 $\frac{\text{mol}}{\text{L}}$, 0.15 $\frac{\text{mol}}{\text{L}}$ to 0.17 $\frac{\text{mol}}{\text{L}}$ for short-chain alcohols and 0.18 $\frac{\text{mol}}{\text{L}}$ for DMF [88]. Therefore, it can be assumed that moist and non-degassed organic solvents contain enough carbon dioxide to explain the formation of the carbonates that we observed. Another source for the input of carbon dioxide and thus carbonates could also be the used acids [89,90]. If we look at the Pourbaix diagram [91,92] of carbon dioxide, we see that formate can be formed from carbonates under the parameters described for the MP process, i.e., standard room temperature and partial pressure for carbon dioxide in ambient air. Due to the reductive basic conditions at the cathode, the carbonates are partially reduced to formates. It is precisely under these conditions that the oxidation of solvents, such as isopropanol and isobutanol, to carboxylic acid-like species seems very unlikely to occur as an explanatory model for the observed C1s XPS (Fig. 10) and Raman spectra (Fig. 7). However, should the solvents used be oxidized anodically and reach the cathode by diffusion, we or comparable studies [48,52,65,80] should have been able to detect these decomposition products. Neither studies in DMF [80] found nitrogen signals in the thin film, nor did we find the typical rotational spectra of short-chain alcohols. As with the carbonates, no conclusive mechanism is described in the literature for the formation of thulium formates by weathering of hydroxides and oxides that may have formed in humid laboratory air. Formate formation during the molecular plating process is the most obvious explanation, while a formation after plating seems to be unlikely. The resulting thin films can therefore be described as a mixture of armorphous basic carbonates and formates.

The chemical conversion of our samples differs significantly from the heat-induced conversion of MP thin films described in literature [46,52]. The oxycarbonate agglomerates reported are known thermal degradation products of carbonates [81] and formates [59]. Thermogravimetric investigations of related carboxylic acid-lanthanide compounds also indicate oxycarbonates as the final product before the

heat-induced transformation into the sesquioxides [71,93]. The chemical transformations we identified after the irradiation with heavy ions cannot be explained by a purely thermal process [29,94], since none of the known decomposition products were detected. Radiation-induced amorphousness could also be a reason for the lack of spectroscopic evidence. The response of the oxides of the lanthanides [95] and actinides [96] to irradiation with swift heavy ions has been extensively investigated for pure crystalline samples. Ion irradiation induces defect formation in the crystal and a loss of O. It would therefore be logical to attribute the chemical transformation of our MP films to a comparable mechanism [97]. This also includes the loss of light volatile elements, like C and O, so that the lanthanide oxide with embedded carbon clusters remain [69]. The relatively strong Raman-signal of the carbon clusters does not yield any information regarding their quantitative contribution to the MP thin film following irradiation. Based on the ion beam analyses, it can be inferred that irradiated thin films exhibit a significantly higher O than C content. Despite extensive research, we were unable to identify a satisfactory explanation for the observation that thin films previously irradiated with Au ions exhibit a reduced degree of morphological change when irradiated with Cl ions, in comparison to those that have not been irradiated.

Future studies would benefit from complementary microscopic techniques that offer sufficient spatial resolution enabling effective analysis despite the challenging morphology of the MP thin films. As the production of superheavy elements relies on actinide, and not on lanthanide targets, the presented studies will ideally also be performed with actinide targets. Such studies, though, require access to modern analytical methods in appropriate licensed nuclear analytical laboratories. These studies will ideally be complemented with irradiations applying higher fluences.

CRediT authorship contribution statement

C.-C. Meyer: Writing – review & editing, Writing – original draft, Project administration, Methodology, Investigation, Funding acquisition, Formal analysis, Data curation, Conceptualization. **E. Artes:** Investigation. **M. Bender:** Investigation. **J. Brötz:** Investigation. **Ch.E. Düllmann:** Writing – review & editing, Supervision, Project administration. **T. Gouder:** Investigation. **E. Jäger:** Investigation. **B. Kindler:** Investigation. **S. Herz:** Investigation. **B. Lommel:** Investigation. **M. Major:** Investigation. **C. Mokry:** Investigation. **F. Munnik:** Investigation. **M. Rapps:** Investigation. **D. Renisch:** Investigation. **J. Runke:** Investigation. **A. Seibert:** Investigation. **C. Trautmann:** Writing – review & editing, Supervision, Project administration. **N. Trautmann:** Supervision, Project administration. **O. Walter:** Investigation. **A. Yakushev:** Project administration, Investigation.

Declaration of Generative AI and AI-assisted technologies in the writing process

In the course of preparing this work, the authors employed the DeepL tool to enhance the readability and linguistic quality of the text. Following the utilization of this tool, the authors conducted a thorough review and editing of the content, assuming full responsibility for the content of the published article.

Declaration of competing interest

The authors declare that they have no known competing financial interests or personal relationships that could have appeared to influence the work reported in this paper.

Acknowledgments

We would like to thank our colleagues from the research reactor TRIGA Mainz for carrying out the neutron activation of the lanthanide standards. We also acknowledge the local support of the mechanical workshop at the TRIGA reactor site Mainz and the financial support from the Helmholtz Institute Mainz. We would like to thank our colleagues from the Department of Materials Science at the Technical University of Darmstadt for their helpful cooperation. The results presented here are based on experiments, which were performed at the beam lines X0 and X8 at the GSI Helmholtzzentrum für Schwerionenforschung, Darmstadt (Germany) in the frame of FAIR Phase-0. This project received funding from the German BMBF (project 05P21UMFN2). We express our gratitude to the Ion Beam Centre of the Helmholtz-Zentrum Dresden-Rossendorf for conducting the ion beam analysis of our samples. Access to the ActUsLab/PAMEC and ActUsLab/FMR facilities was granted under the Framework of access to the Joint Research Centre Physical Research Infrastructures of the European Commission (Research Infrastructure Access Agreement № 2020-1-RD-ActUsLab-FMR Targets-SHE1 (AUL-233) and 2020-1-RD-ActUsLab-PAMEC Targets-SHE2 (AUL-228)). Any opinions, findings and conclusions or recommendations expressed in this paper are those of the authors and do not necessarily reflect those of the European Commission.

Data availability

Data will be made available on request.

References

[1] S. Hofmann, Synthesis and properties of isotopes of the transactinides, Radiochim. Acta 107 (9–11) (2019) 879–915.
[2] S. Dmitriev, A. Popeko, High-power radioactive targets as one of the key problems in further development of the research program on synthesis of new superheavy elements, J. Radioanal. Nucl. Chem. 305 (2015) 927–933.
[3] Y.T. Oganessian, S.N. Dmitriev, Synthesis and study of properties of superheavy atoms. Factory of superheavy elements, Russ. Chem. Rev. 85 (2016) 901.
[4] O.R. Smits, C.E. Düllmann, P. Indelicato, W. Nazarewicz, P. Schwerdtfeger, The quest for superheavy elements and the limit of the periodic table, Nat. Rev. Phys. 6 (2) (2024) 86–98.
[5] A. Såmark-Roth, D. Cox, D. Rudolph, L. Sarmiento, B. Carlsson, J. Egido, P. Golubev, J. Heery, A. Yakushev, S. Åberg, et al., Spectroscopy along flerovium decay chains: Discovery of Ds-280 and an excited state in Cn-282, Phys. Rev. Lett. 126 (3) (2021) 032503.
[6] D. Rudolph, U. Forsberg, P. Golubev, L. Sarmiento, A. Yakushev, L.-L. Andersson, A. Di Nitto, C.E. Düllmann, J. Gates, K. Gregorich, et al., Spectroscopy of element 115 decay chains, Phys. Rev. Lett. 111 (11) (2013) 112502.
[7] A. Yakushev, J. Khuyagbaatar, C.E. Düllmann, M. Block, R. Cantemir, D. Cox, D. Dietzel, F. Giacoppo, Y. Hrabar, M. Iliaš, et al., Manifestation of relativistic effects in the chemical properties of nihonium and moscovium revealed by gas chromatography studies, Front. Chem. 12 (2024) 1474820.
[8] Y.T. Oganessian, F.S. Abdullin, C. Alexander, J. Binder, R.A. Boll, S. Dmitriev, J. Ezold, K. Felker, J. Gostic, R.K. Grzywacz, et al., Experimental studies of the ^{249}Bk+ ^{48}Ca reaction including decay properties and excitation function for isotopes of element 117, and discovery of the new isotope ^{277}mt, Phys. Rev. C—Nucl. Phys. 87 (5) (2013) 054621.
[9] B. Lommel, C.E. Düllmann, B. Kindler, D. Renisch, Status and developments of target production for research on heavy and superheavy nuclei and elements, Eur. Phys. J. 59 (2) (2023) 14.
[10] C. Stodel, Methods of targets characterization, in: EPJ Web of Conferences, Vol. 229, EDP Sciences, 2020, p. 02001.
[11] P. Steinegger, Open questions on chemistry in the synthesis and characterization of superheavy elements, Commun. Chem. 4 (1) (2021) 1–4.
[12] C.E. Düllmann, E. Artes, A. Dragoun, R. Haas, E. Jäger, B. Kindler, B. Lommel, K.-M. Mangold, C.-C. Meyer, C. Mokry, et al., Advancements in the fabrication and characterization of actinide targets for superheavy element production, J. Radioanal. Nucl. Chem. 332 (5) (2023) 1505–1514.
[13] C.-C. Meyer, E. Artes, M. Bender, J. Brötz, C.E. Düllmann, C. Haese, E. Jäger, B. Kindler, B. Lommel, M. Major, M. Rapps, D. Renisch, C. Trautmann, A. Yakushev, Fabrication, swift heavy ion irradiation, and damage analysis of lanthanide targets, Radiochim. Acta 111 (11) (2023) 801–815.
[14] K. Morita, SHE research at RIKEN/garis, Nucl. Phys. A 944 (2015) 30–61.

[15] C. Stodel, J.F. Libin, C. Marry, F. Lutton, M.G. Saint-Laurent, B. Bastin, J. Piot, E. Clement, S. Le Moal, V. Morel, et al., High intensity targets stations for S 3, J. Radioanal. Nucl. Chem. 305 (2015) 761–767.

[16] S. Dmitriev, M. Itkis, Y.T. Oganessian, Status and perspectives of the dubna superheavy element factory, in: EPJ Web of Conferences, Vol. 131, EDP Sciences, 2016, p. 08001.

[17] H. Haba, A new period in superheavy-element hunting, Nat. Chem. 11 (1) (2019) 10–13.

[18] C.E. Düllmann, M. Block, F.P. Heßberger, J. Khuyagbaatar, B. Kindler, J.V. Kratz, B. Lommel, G. Münzenberg, V. Pershina, D. Renisch, et al., Five decades of GSI superheavy element discoveries and chemical investigation, Radiochim. Acta 110 (6–9) (2022) 417–439.

[19] E. Artes, C.E. Düllmann, C.-C. Meyer, D. Renisch, The process of molecular plating and the characteristics of the produced thin films–what we have learned in 60 years and what is still unknown, in: EPJ Web of Conferences, Vol. 285, EDP Sciences, 2023, p. 03001.

[20] S. Hofmann, S. Heinz, R. Mann, J. Maurer, J. Khuyagbaatar, D. Ackermann, S. Antalic, W. Barth, M. Block, H. Burkhard, et al., The reaction ^{48}Ca + ^{248}Cm → ^{296}116* studied at the GSI-SHIP, Eur. Phys. J. 48 (5) (2012) 1–23.

[21] N. Brewer, V. Utyonkov, K.P. Rykaczewski, Y.T. Oganessian, F.S. Abdullin, R. Boll, D.J. Dean, S. Dmitriev, J.G. Ezold, L. Felker, et al., Search for the heaviest atomic nuclei among the products from reactions of mixed-Cf with a ^{48}Ca beam, Phys. Rev. C: Nucl. Phys. 98 (2) (2018) 024317.

[22] A. Yakushev, J.M. Gates, A. Türler, M. Schädel, C.E. Düllmann, D. Ackermann, L.-L. Andersson, M. Block, W. Brüchle, J. Dvorak, et al., Superheavy element flerovium (element 114) is a volatile metal, Inorg. Chem. 53 (3) (2014) 1624–1629.

[23] A. Yakushev, L. Lens, C.E. Düllmann, J. Khuyagbaatar, E. Jäger, J. Krier, J. Runke, H. Albers, M. Asai, M. Block, et al., On the adsorption and reactivity of element 114, flerovium, Front. Chem. 10 (2022) 976635.

[24] D.M. Cox, A. Såmark-Roth, D. Rudolph, L.G. Sarmiento, R.M. Clark, J.L. Egido, P. Golubev, J. Heery, A. Yakushev, S. Åberg, H.M. Albers, M. Albertsson, M. Block, H. Brand, T. Calverley, R. Cantemir, B.G. Carlsson, C.E. Düllmann, J. Eberth, C. Fahlander, U. Forsberg, J.M. Gates, F. Giacoppo, M. Götz, S. Götz, R.-D. Herzberg, Y. Hrabar, E. Jäger, D. Judson, J. Khuyagbaatar, B. Kindler, I. Kojouharov, J.V. Kratz, J. Krier, N. Kurz, L. Lens, J. Ljungberg, B. Lommel, J. Louko, C.-C. Meyer, A. Mistry, C. Mokry, P. Papadakis, E. Parr, J.L. Pore, I. Ragnarsson, J. Runke, M. Schädel, H. Schaffner, B. Schausten, D.A. Shaughnessy, P. Thörle-Pospiech, N. Trautmann, J. Uusitalo, Spectroscopy along flerovium decay chains. II. Fine structure in odd-A ^{289}Fl, Phys. Rev. C: Nucl. Phys. 107 (2023) L021301.

[25] D. Cox, A. Såmark-Roth, D. Rudolph, L. Sarmiento, C. Fahlander, U. Forsberg, P. Golubev, J. Heery, A. Yakushev, H. Albers, et al., Spectroscopic tools applied to flerovium decay chains, in: J. Phys. Conf. Ser, Vol. 1643, IOP Publishing, 2020, 012125.

[26] R. Haas, C.-C. Meyer, S. Böhland, C.E. Düllmann, J. Mäder, K. Tinschert, ODIn - a setup for off-line deposit irradiations of thin layers for nuclear physics applications, Nucl. Instrum. Methods Phys. Res. Sect. A 957 (2020) 163366.

[27] C.-C. Meyer, A. Dragoun, C.E. Düllmann, R. Haas, E. Jäger, B. Kindler, B. Lommel, A. Prosvetov, M. Rapps, D. Renisch, et al., Chemical conversions in lead thin films induced by heavy-ion beams at Coulomb barrier energies, Nucl. Instrum. Methods Phys. Res. Sect. A (2022) 166365.

[28] K. Eberhardt, C.E. Düllmann, R. Haas, C. Mokry, J. Runke, P. Thörle-Pospiech, N. Trautmann, Actinide targets for fundamental research in nuclear physics, in: AIP Conference Proceedings, Vol. 1962, AIP Publishing LLC, 2018, 030009.

[29] D. Mayorov, E. Tereshatov, T. Werke, M. Frey, C. Folden III, Heavy-ion beam induced effects in enriched gadolinium target films prepared by molecular plating, Nucl. Instrum. Methods Phys. Res. Sect. B 407 (2017) 256–264.

[30] S. Cotton, Lanthanide and Actinide Chemistry, John Wiley & Sons, Ltd, 2013.

[31] A. Vascon, S. Santi, A. Isse, T. Reich, J. Drebert, H. Christ, C.E. Düllmann, K. Eberhardt, Elucidation of constant current density molecular plating, Nucl. Instrum. Methods Phys. Res. Sect. A 696 (2012) 180–191.

[32] J. Runke, C.E. Düllmann, K. Eberhardt, P. Ellison, K. Gregorich, S. Hofmann, E. Jäger, B. Kindler, J. Kratz, J. Krier, et al., Preparation of actinide targets for the synthesis of the heaviest elements, J. Radioanal. Nucl. Chem. 299 (2) (2014) 1081–1084.

[33] P. Caro, J. Sawyer, L. Evning, The infrared spectra of rare earth carbonates, Spectrochim. Acta A 28 (6) (1972) 1167–1173.

[34] D.E. Newbury, N.W. Ritchie, Performing elemental microanalysis with high accuracy and high precision by scanning electron microscopy/silicon drift detector energy-dispersive X-ray spectrometry (SEM/SDD-EDS), J. Mater. Sci. 50 (2) (2015) 493–518.

[35] A. Gurbich, SigmaCalc recent development and present status of the evaluated cross-sections for IBA, Nucl. Instrum. Methods Phys. Res. Sect. B 371 (2016) 27–32.

[36] N. Barradas, C. Jeynes, R. Webb, Simulated annealing analysis of rutherford backscattering data, Appl. Phys. Lett. 71 (2) (1997) 291–293.

[37] L. Burgio, R.J. Clark, Library of FT-Raman spectra of pigments, minerals, pigment media and varnishes, and supplement to existing library of Raman spectra of pigments with visible excitation, Spectrochim. Acta A 57 (7) (2001) 1491–1521.

[38] M. Wojdyr, Fityk: A general-purpose peak fitting program, J. Appl. Crystallogr. 43 (5–1) (2010) 1126–1128.

[39] F. Menges, Spectragryph-optical spectroscopy software, version 1.2. 14, 2020, 2020.

[40] N. Fairley, Casaxps VAMAS processing software, 2010, http://Www.Casaxps.Com.

[41] D.R. Baer, K. Artyushkova, H. Cohen, C.D. Easton, M. Engelhard, T.R. Gengenbach, G. Greczynski, P. Mack, D.J. Morgan, A. Roberts, XPS guide: Charge neutralization and binding energy referencing for insulating samples, J. Vac. Sci. Technol. A 38 (3) (2020) 031204.

[42] C.D. Easton, C. Kinnear, S.L. McArthur, T.R. Gengenbach, Practical guides for x-ray photoelectron spectroscopy: Analysis of polymers, J. Vac. Sci. Technol. A 38 (2) (2020) 023207.

[43] F. Kurth, J. Froemel, S. Tanaka, M. Esashi, T. Gessner, Electroplating of neodymium iron alloys, in: 2016 IEEE 11th Annual International Conference on Nano/Micro Engineered and Molecular Systems, NEMS, IEEE, 2016, pp. 405–408.

[44] D. Liebe, K. Eberhardt, W. Hartmann, T. Häger, A. Hübner, J. Kratz, B. Kindler, B. Lommel, P. Thörle, M. Schädel, et al., The application of neutron activation analysis, scanning electron microscope, and radiographic imaging for the characterization of electrochemically deposited layers of lanthanide and actinide elements, Nucl. Instrum. Methods Phys. Res. Sect. A 590 (1–3) (2008) 145–150.

[45] M.N. Torrico, R.A. Boll, M. Matos, Electrodeposition of actinide compounds from an aqueous ammonium acetate matrix: Experimental development and optimization, Nucl. Instrum. Methods Phys. Res. Sect. A 790 (2015) 64–69.

[46] J.D. Burns, K.G. Myhre, N.J. Sims, D.W. Stracener, R.A. Boll, Effects of annealing temperature on morphology and thickness of samarium electrodeposited thin films, Nucl. Instrum. Methods Phys. Res. Sect. A 830 (2016) 95–101.

[47] K.G. Myhre, J.D. Burns, N.J. Sims, D.W. Stracener, R.A. Boll, Effects of annealing on fission fragment release from electrodeposited cf-252 thin-films, Nucl. Instrum. Methods Phys. Res. Sect. A 955 (2020) 163282.

[48] A. Vascon, S. Santi, A. Isse, A. Kühnle, T. Reich, J. Drebert, K. Eberhardt, C.E. Düllmann, Smooth crack-free targets for nuclear applications produced by molecular plating, Nucl. Instrum. Methods Phys. Res. Sect. A 714 (2013) 163–175.

[49] J. Lodermeyer, M. Multerer, M. Zistler, S. Jordan, H.J. Gores, W. Kipferl, E. Diaconu, M. Sperl, G. Bayreuther, Electroplating of dysprosium, electrochemical investigations, and study of magnetic properties, J. Electrochem. Soc. 153 (4) (2006) C242.

[50] L. Benedik, G. Sibbens, A. Moens, R. Eykens, M. Nečemer, S. Škapin, P. Kump, Preparation of thick uranium layers on aluminium and stainless steel backings, Appl. Radiat. Isot. 87 (2014) 238–241.

[51] L. Sanchez-Cupido, J.M. Pringle, A.L. Siriwardana, A. Unzurrunzaga, M. Hilder, M. Forsyth, C. Pozo-Gonzalo, Water-facilitated electrodeposition of neodymium in a phosphonium-based ionic liquid, J. Phys. Chem. Lett. 10 (2) (2019) 289–294.

[52] J. Choi, Y.H. Chung, Preparation of lanthanum oxide and lanthanum oxycarbonate layers on titanium by electrodeposition with organic solution, J. Nanomater. 2016 (2016) 28.

[53] K. Myhre, J. Burns, H. Meyer, N. Sims, R. Boll, Samarium electrodeposited acetate and oxide thin films on stainless steel substrate characterized by XPS, Surf. Sci. Spectra 23 (1) (2016) 70–81.

[54] L. Spiridigliozzi, M. Bortolotti, G. Accardo, A. Vergara, D. Frattini, C. Ferone, R. Cioffi, G. DellAgli, An in-depth multi-technique characterization of rare earth carbonates–$RE_2(CO_3)_3 \cdot 2\ h_2O$ –owning tengerite-type structure, J. Rare Earths 40 (8) (2022) 1281–1290.

[55] F.A. Andersen, L. Brecevic, et al., Infrared spectra of amorphous and crystalline calcium carbonate, Acta Chem. Scand. 45 (10) (1991) 1018–1024.

[56] U. Wehrmeister, A.L. Soldati, D. Jacob, T. Häger, W. Hofmeister, Raman spectroscopy of synthetic, geological and biological vaterite: A Raman spectroscopic study, J. Raman Spectrosc. 41 (2) (2010) 193–201.

[57] M. Hämmer, H.A. Höppe, Crystalline orthorhombic Ln $[CO_3][OH]$(Ln=La, Pr, Nd, Sm, Eu, Gd) compounds hydrothermally synthesised with CO_2 from air as carbonate source, Z. Naturforsch. B: Chem. Sci. 74 (1) (2019) 59–70.

[58] V. Kartha, S. Venkateswaran, Vibrational spectra and normal vibrations of rare earth formates, Spectrochim. Acta A 37 (11) (1981) 927–934.

[59] M. Moura, A. Ayala, J. Mendes Filho, I. Guedes, C. Paschoal, A. Leyva, G. Polla, D. Vega, P. De Perazzo, H. Lanza, Thermal behavior in $Pr(HCOO)_3$ crystals, J. Raman Spectrosc. 35 (2) (2004) 159–164.

[60] E. Silva, M. Moura, A. Ayala, I. Guedes, G. Polla, D. Vega, D. Tobia, M. Saleta, Vibrational modes of rare-earth formates, J. Raman Spectrosc. 40 (8) (2009) 954–957.

[61] G. Herzberg, Molecular Spectra and Molecular Structure, D. van Nostrand, 1945.

[62] L. Song, M. Rong-jun, IR of hydrated rare Earth carbonates, Sci. Technol. Eng. 7 (7) (2007) 36.

[63] L. Jin, PrÉparation de Cibles D'Uranium: comprÉhension Du ProcÉdÉ D'ÉlectroprÉcipitation Pour Optimiser Les Conditions OpÉratoires (Ph.D. thesis), Université Paris-Saclay, 2021.

[64] S. Sadi, A. Paulenova, P. Watson, W. Loveland, Growth and surface morphology of uranium films during molecular plating, Nucl. Instrum. Methods Phys. Res. Sect. A 655 (1) (2011) 80–84.

[65] G. Sibbens, M. Ernstberger, T. Gouder, M. Marouli, A. Moens, A. Seibert, D. Vanleeuw, M.V. Zúñiga, T. Wiss, M. Zampella, et al., Morphological and compositional study of ^{238}U thin film targets for nuclear experiments, in: AIP Conference Proceedings, Vol. 1962, AIP Publishing LLC, 2018, 030007.
[66] A. Ölcer, J. Drebert, T. Reich, XPS-Oberflächenanalyse von elektrochemisch hergestellten Urantargets, Tech. rep., Institut für Kernchemie, Johannes Gutenberg-Universität Mainz (Germany), 2007.
[67] T. Smirnova, V. Volodin, M. Lebedev, V. Belyi, Raman scattering spectroscopy of inclusions of carbon in Al_2O_3 films and its solid solutions with hfo_2, Opt. Spectrosc. 110 (1) (2011) 55–59.
[68] A.C. Ferrari, J. Robertson, Interpretation of Raman spectra of disordered and amorphous carbon, Phys. Rev. B: Condens. Matter 61 (20) (2000) 14095.
[69] S. Belaya, V. Bakovets, A. Boronin, S. Koshcheev, M. Lobzareva, I. Korolkov, P. Stabnikov, Terbium oxide films grown by chemical vapor deposition from terbium (III) dipivaloylmethanate, Inorg. Mater. 50 (4) (2014) 379–386.
[70] J. Hodkiewicz, Characterizing graphene with Raman spectroscopy, Thermo Fish. Sci. (2010) 51946.
[71] J.-C. Grivel, Thermal decomposition of $Ln(C_2H_5CO_2)$ 3· H_2O (Ln=Ho, Er, Tm and Yb), J. Therm. Anal. Calorim. 109 (1) (2012) 81–88.
[72] P.E. Larson, M.A. Kelly, Surface charge neutralization of insulating samples in X-ray photoemission spectroscopy, J. Vac. Sci. Technol. A 16 (6) (1998) 3483–3489.
[73] J. Cazaux, Mechanisms of charging in electron spectroscopy, J. Electron. Spectrosc. Relat. Phenom. 105 (2–3) (1999) 155–185.
[74] G. Greczynski, L. Hultman, The same chemical state of carbon gives rise to two peaks in X-ray photoelectron spectroscopy, Sci. Rep. 11 (1) (2021) 1–5.
[75] B.V. Crist, XPS database entry for Tm_2O_3, 2022, https://xpsdatabase.com/thulium-spectra-tm2o3-thulium-oxide/. (Accessed 10 September 2024).
[76] R. Bolotovsky, A. Bulkin, G. Krutov, V. Kudryashev, V. Trunov, V. Ul'yanov, O. Antson, P. Hiismäki, H. Pöyry, A. Tiitta, et al., Neutron diffraction study of the crystal structure of rare-earth and yttrium anhydrous deuterated formates, Solid State Commun. 76 (8) (1990) 1045–1049.
[77] D. Zagorac, H. Müller, S. Ruehl, J. Zagorac, S. Rehme, Recent developments in the inorganic crystal structure database: Theoretical crystal structure data and related features, J. Appl. Crystallogr. 52 (5) (2019) 918–925.
[78] B. Lommel, W. Brüchle, K. Eberhardt, W. Hartmann, A. Hübner, B. Kindler, J.V. Kratz, D. Liebe, M. Schädel, J. Steiner, Backings and targets for chemical and nuclear studies of transactinides with TASCA, Nucl. Instrum. Methods Phys. Res. Sect. A 590 (1–3) (2008) 141–144.
[79] S. Sadi, A. Paulenova, W. Loveland, P. Watson, J. Greene, S. Zhu, G. Zinkann, Surface morphology and phase stability of titanium foils irradiated with 136 MeV ^{136}Xe, Nucl. Instrum. Methods Phys. Res. Sect. B 328 (2014) 78–83.
[80] K.G. Myhre, J.C. Delashmitt, N.J. Sims, S.M. Van Cleve, R.A. Boll, Samarium thin films molecular plated from N, N-dimethylformamide characterized by XPS, Surf. Sci. Spectra 25 (2) (2018) 024003.
[81] T. Kutty, I. Mohamed, J. Tareen, Hydrothermal phase equilibria in Ln_2O_3-H_2O-CO_2 systems for Tm, Yb and Lu, Mater. Chem. Phys. 10 (5) (1984) 425–441.
[82] S. Bernal, G. Blanco, J. Gatica, J. Pérez-Omil, J. Pintado, H. Vidal, Chemical reactivity of binary rare earth oxides, in: Binary Rare Earth Oxides, Springer Netherlands, Dordrecht, 2004, pp. 9–55.
[83] A. Orera, G. Larraz, M. Sanjuán, Spectroscopic study of the competition between dehydration and carbonation effects in la_2O_3-based materials, J. Eur. Ceram. Soc. 33 (11) (2013) 2103–2110.
[84] P.G. Hansen, The conditions for electrodeposition of insoluble hydroxides at a cathode surface: A theoretical investigation, J. Inorg. Nucl. Chem. 12 (1–2) (1959) 30–37.
[85] M. Ramaniah, R. Singh, S. Awasthi, S. Prakash, Studies on electrodeposition of actinide elements from non-aqueous medium, Int. J. Radiat. Appl. Instrum. Part A 26 (11) (1975) 648–650.
[86] M. Crespo, A review of electrodeposition methods for the preparation of alpha-radiation sources, Appl. Radiat. Isot. 70 (1) (2012) 210–215.
[87] Y. He, L. Han, C. Wang, Q. Chen, M.M. Sartin, G. Li, R. Hu, J. Tu, X. Xie, Y. Yang, et al., Molecular plating of actinide compounds on wafer-scale aluminum substrate, J. Alloys Compd. 878 (2021) 160393.
[88] K. Izutsu, Electrochemistry in Nonaqueous Solutions, John Wiley & Sons, Weinheim, 2009.
[89] G. Geffcken, Beiträge zur kenntnis der löslichkeitsbeeinflussung, Z. Phys. Chem. 49 (1) (1904) 257–302.
[90] O. Ustinov, A. Schadrin, O. Shmidt, O. Shudegova, Study of carbon dioxide solubility in nitric acid and metal nitrates solutions for estimation of carbon-14 distribution between gas phase and solution during dissolution of spent nuclear fuel, 17. Radiochem. Conf. Marian. Lazne, Bookl. Abstr. 17 (98) (2014) 11. - 16. May.
[91] Y.I. Hori, Electrochemical CO_2 reduction on metal electrodes, in: Modern Aspects of Electrochemistry, Springer, New York, 2008, pp. 89–189.
[92] M. König, J. Vaes, E. Klemm, D. Pant, Solvents and supporting electrolytes in the electrocatalytic reduction of CO_2, IScience 19 (2019) 135–160.
[93] G.A. Hussein, G.A. Mekhemer, B.A. Balboul, Formation and surface characterization of thulium oxide catalysts, PCCP 2 (9) (2000) 2033–2038.
[94] R. Sagaidak, Effects of beam wobbling and target rotation on the target temperature in experiments with intense heavy ion beams, Phys. Rev. Accel. Beams 24 (8) (2021) 083001.
[95] C.L. Tracy, M. Lang, F. Zhang, C. Trautmann, R.C. Ewing, Phase transformations in Ln_2O_3 materials irradiated with swift heavy ions, Phys. Rev. B: Condens. Matter 92 (17) (2015) 174101.
[96] C.L. Tracy, M. Lang, J.M. Pray, F. Zhang, D. Popov, C. Park, C. Trautmann, M. Bender, D. Severin, V.A. Skuratov, et al., Redox response of actinide materials to highly ionizing radiation, Nat. Commun. 6 (1) (2015) 1–9.
[97] C. Stodel, M. Toulemonde, C. Fransen, B. Jacquot, E. Clément, G. Fremont, M. Michel, C. Dufour, Thermal spike model applied to thin targets irradiated with swift heavy ion beams at few MeV/u, in: EPJ Web of Conferences, Vol. 229, EDP Sciences, 2020, p. 05001.